J Sci Comput (2017) 71:839–874
DOI 10.1007/s10915-016-0323-5

A Grid-Insensitive LDA Method on Triangular Grids Solving the System of Euler Equations

Hossain Chizari[1] · **Farzad Ismail**[1]

Received: 28 April 2016 / Revised: 3 November 2016 / Accepted: 10 November 2016 /
Published online: 17 November 2016

Abstract The performance of the classic upwind-type residual distribution (RD) methods on skewed triangular grids are rigorously investigated in this paper. Based on an improved signals distribution, an improved second order RD method based on the LDA approach is proposed to faithfully replicate the flow physics on skewed triangular grids. It will be mathematically and numerically shown that the improved LDA method is found to have minimal accuracy variations when grids are skewed compared to classic RD and cell vertex finite volume methods on scalar equations and system of Euler equations.

Keywords Residual distribution · LDA · Skewed triangular grids · Cell-vertex finite volume · Hyperbolic conservation laws

1 Introduction

Historically, the residual distribution concept developed in two different research paths. The first was the study by Hall, Morton and collaborators in 1980's which focused on the cell-vertex finite volume methods [1–3]. The second path was concerned with the physics of the PDE by Roe [4]. In 1982, Roe [4] proposed a framework of an multidimensional upwind residual distribution (RD) but merely for the scalar convection problem. The generalization for a system of equation in two dimensions was done by Abgrall [5,6], implementing the idea on the Euler equations. The current status and future trends of the RD methods are described in details by Abgrall [7,8] and the references therein.

One of the purposes of using RD methods was to obtain more accurate solutions on unstructured triangular grids. Among the motivations of developing the RD methods are

✉ Farzad Ismail
aefarzad@usm.my

Hossain Chizari
hc12_aer008@student.usm.my

[1] School of Aerospace Engineering, Engineering Campus, Universiti Sains Malaysia, 14300 Pulau Penang, Malaysia

to faithfully mimic multidimensional physics and keep a compact stencil compared to the finite volume (FV) methods. These include the work of [9] and it was briefly shown that RD methods are insensitive to randomized grids [10,11]. The works of [12] provide a rigorous analytical discussion of the performance of RD and FV on structured triangular grids but limited to only the scalar problems. [13] provided the comparison on the system of Euler equations but merely demonstrated through the numerical results. Both works noted that RD methods are affected by grid deterioration but at a much lesser rate compared to FV methods. An attempt to accurately develop an RD method on skewed triangular grids is almost non-existent in the literature. Most of the developments for RD methods are based on ideal or regular grids [6,14,15] although most recently there have been some developments of Streamline-Upwind-Petrov–Galerkin (SUPG) RD methods on stretched triangular grids [16] solving the advection–diffusion and potential flow equations.

In this paper, we intend to analyze in-depth the performance of RD methods on skewed triangular grids. Then we aim to develop an RD method based on the LDA approach which would include a more accurate signal distribution to the nodes when the grids are skewed. This newly proposed LDA approach is intended to preserve accuracy for a large range of grid skewness on isotropic and anisotropic grids. For a start, the focus of this paper would be on two dimensional steady state equations. The analysis begins with the scalar equations followed by the system of Euler equations. The fully unstructured (anisotropic) grids will be used for the Euler test case, particularly for the Ringleb flow and the subsonic flow over a two-dimensional circular cylinder.

2 Classic RD Methods for Scalar Equations

Consider the general two dimensional hyperbolic scalar equation.

$$u_t + \vec{\nabla} \cdot \vec{F} = 0, \tag{1}$$

where t is time, F is the flux as a function of u which is the dependent variable. The total (ϕ_T^τ) residual in cell τ is defined as,

$$\phi_T^\tau = \oint_{\partial\tau} \vec{F} \cdot \hat{n} dS \tag{2}$$

where the $\hat{n}$ is the inward unit normal vector and dS is the differential length of the element along the border of the cell (Fig. 1). Applying the trapezoidal integration rule in a cell,

$$\phi_T^\tau = \frac{1}{2} \sum_p \vec{F}_p \cdot \vec{N}_p, \quad p = i, j, k \tag{3}$$

where $\vec{N}_i$ is the inward normal of each edge scaled with the length and, $\vec{F}_i$ is the flux vector of the node in front of the ith edge. In the RD methods, the total residual is spread to points (nodes) and the approaches will be discussed in the following subsections. We start with the classic RD methods followed by the new distribution approach. The scope will be on first and second order upwind-type methods since this is a proof-of-concept paper. Herein, the governing models for Eq. (1) are $\vec{F} = (a, b)u$ for the linear and $\vec{F} = (u^2/2, u)$ for the nonlinear scalar equations. Define,

$$k_i = \frac{1}{2} \vec{\lambda}_{\text{ave}} \cdot \vec{N}_i \tag{4}$$

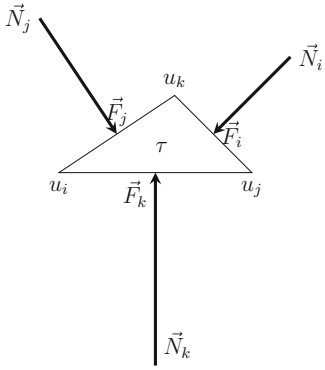

Fig. 1 The total cell residual (τ in the cell domain for integration)

And,

$$k_i^+ = \begin{cases} k_i & k_i \geq 0 \\ 0 & k_i < 0 \end{cases}, \quad k_i^- = \begin{cases} 0 & k_i \geq 0 \\ k_i & k_i < 0 \end{cases} \tag{5}$$

where $\vec{\lambda}_{\text{ave}}$ is the average characteristic vector within the cell. For a linear case, $\vec{\lambda}_{\text{ave}}$ is constant but our formulation will also cater for the nonlinear case.

2.1 N-scheme

The classic N-scheme formulation [7] is shown in Eq. (6). It should be mentioned that the k_i is referring to edge i within an element (τ) and, u_i refers to the values of point i in front of the edge i. According to Eq. (4),

$$\phi_i^\tau = k_i^+ \left(u_i - \hat{u}\right), \quad \hat{u} = \left(\sum_p k_p^-\right)^{-1} \sum_p k_p^- u_p, \quad p = i, j, k \tag{6}$$

Note that the averaging type in Eq. (4) has to be specific in order to achieve conservation. For instance, in the Burgers' equation it should be the arithmetic average of u [17].

2.2 LDA

The LDA formulation for scalar equation is,

$$\phi_i^\tau = \beta_i \phi_T^\tau, \quad \beta_i = k_i^+ \left(\sum_p k_p^+\right)^{-1}, \quad p = i, j, k \tag{7}$$

where ϕ_T^τ is the total residual of the cell. Therefore, the averaging type in Eq. (4) would not affect the conservation because of the following fact.

$$\sum_p \beta_p = 1 \tag{8}$$

There are two scenarios in LDA; the 1-target and 2-target cell which are distinguished by the $k_{i,j,k}^+$. If a cell has one (two) non-zero $k_{i,j,k}^+$ then it will be 1-target (2-target).

2.3 Lax–Wendroff

For the Lax–Wendroff scheme like the LDA is also Linearity Preserving (LP) in which the signals are in the following form.

$$\phi_i^\tau = \beta_i \phi_T^\tau, \quad \beta_i = \frac{1}{3} + \frac{\Delta t}{2A^\tau} k_i \tag{9}$$

A^τ is the element area and, Δt is element delta time. Based on [17],

$$\Delta t = \nu_c \left(\frac{2A^\tau}{\sum_p |k_p|} \right), \quad p = i, j, k \tag{10}$$

which leads to,

$$\beta_i = \frac{1}{3} + \nu_c \frac{k_i}{\sum_p |k_p|} \tag{11}$$

The ν_c is the cell CFL number.

3 Weighted RD Approach

3.1 Geometrical Aspects on Skewed Grids for Scalar

In the classic signal distribution, the projections of the characteristic vector normal to each edge is required to find the signal portion. Define,

$$\vec{\lambda}_p = \left(\vec{\lambda} \cdot \hat{n}_p \right) \hat{n}_p, \quad p = i, j, k \tag{12}$$

where $\vec{\lambda}_p$ shows the vector projection of the characteristic vector ($\vec{\lambda}$) along the inward normal of edge p. If the length of this projection ($\vec{\lambda} \cdot \hat{n}_p$) becomes positive it means that the characteristic is coming into the cell and vice versa. Hence, number of the positive lengths in a cell will illustrate the 1-target or 2-target cell type. Thus, similar to the definition of k^+, one can define,

$$\vec{\lambda}_p^+ = \begin{cases} \vec{\lambda}_p & \vec{\lambda} \cdot \hat{n}_p \geq 0 \\ 0 & \vec{\lambda} \cdot \hat{n}_p < 0 \end{cases} \tag{13}$$

3.1.1 Case: 1-Target

Assume the 1-target case for a triangle (Fig. 2a). According to the definition of $\vec{\lambda}_p^+$, only one of them will be non-zero for a 1-target cell. As it can be seen from the Fig. 2a, even though the $\vec{\lambda}_k^+$ is pointing into a midpoint along the edge somewhere in between points i and k for a skewed grid nonetheless, all the residual is going to point k. This may not be the best way to distribute the signals. We propose that the signals be distributed to points i and k as shown in Fig. 2b. As a result, the 1-target now becomes a 2-target cell with this new approach. It is obvious that for an equilateral element the point m will be identical to the k, hence we can deduce that the new approach would recover the classic 1-target for equilateral triangles (and for lowly skewed triangles). Note that $\vec{\lambda}$ is based on some form of averaging within the cell and located at the geometrical center of the triangle ensure that this idea can also be extended to nonlinear Burgers' equation.

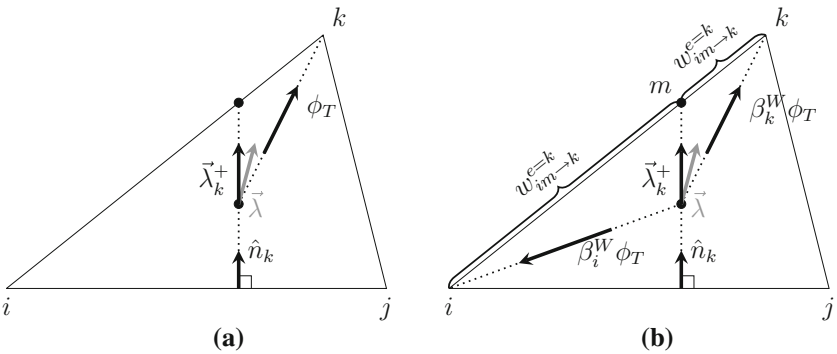

Fig. 2 Classic 1-target element ($\vec{\lambda}_{i,j}^+ = 0$) with two signal distribution. Note that the signals are distributed to point i ($\beta_i^W \phi_T$) and point k ($\beta_k^W \phi_T$) accordingly for which the weights $\beta_{i,k}^W$ are to be determined. **a** Classic signal distribution, **b** Weighted signal distribution

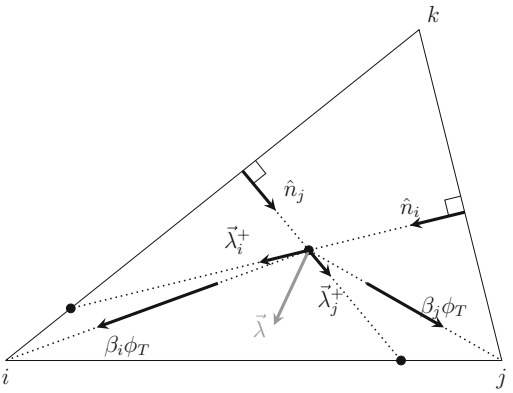

Fig. 3 Classic 2-target element ($\vec{\lambda}_k^+ = 0$) with classic signal distribution

3.1.2 Case: 2-Target

For the 2-target scenario the same approach is applied. The pivot point of the cell will be the geometrical center and from there the residual is distributed based on the upwind idea. Again, we use some kind of an averaging for the cell. Note that for an equilateral grid the weighted approach will recover the classic upwind approach thus, we merely discuss a skewed grid condition here. In Fig. 3, the classic distribution is shown for a skewed grid. Similar to the 1-target case, the projections of the characteristic vector are not pointing at the main points i, j, k, yet the signals are solely going to the respective 2-target points. However, in the weighted approach (Fig. 4) each of the two-target signals will be distributed to the nodes that share the element edge for which the projected characteristic vector are pointing at. This will cause the 2-target case to be a 3-target case (loss of upwind) for highly skewed grids. However, for an equilateral grids a or a minimally skewed grids, the 2-target case would remain 2-target.

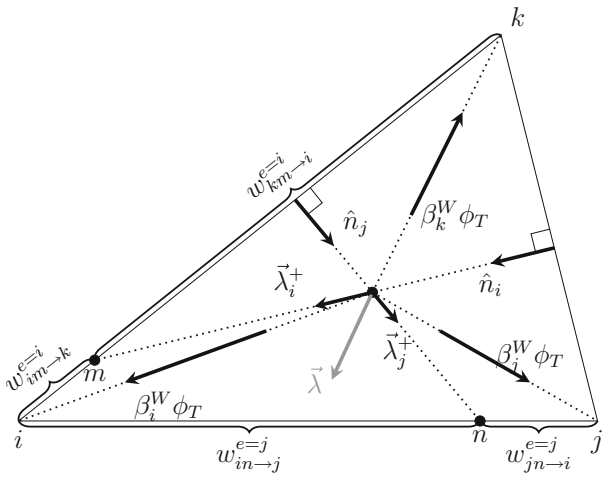

Fig. 4 Classic 2-target element ($\vec{\lambda}^+_k = 0$) with weighted signal distribution

3.2 Weighted Distribution

In this section, we are address precise aspects of the weighted approach. In order to construct a less sensitive signal distribution, according to Figs. 2b and 4, the ratios of

$$w^{e=(\text{edge number})}_{(\text{distance ratio})\to(\text{point of interest})}, \quad \text{point of intreset} = i, j, k \tag{14}$$

are required. Note that the edge number e is defined as i, j, k which are the edges in front of i, j, k points, respectively. For a skewed grid, the first point of interest of the inward normal direction (point m) will be on some edge which is not a nodal point, necessarily. This will require a weighted distribution between the nodes that connect the particular edge. Distributing with weighted idea will produce more accurate distribution of the signals.

It is clear that for all three edges the w should be calculated. Thus, we have nine values for w in one element but some of them maybe zeros depending on the grid orientation. The zero weights are discussed after Lemma 3.1 and 3.2. In order to find the weights (w) we have to first construct the geometrical foundation.

Lemma 3.1 *Consider an arbitrary vector $\vec{d}$ starts from a geometrical center of a triangle* (Fig. 5). *Assume the total area is A^τ, the area ratios could be shown as,*

$$\frac{A_p}{A^\tau} = \frac{1}{3} + \frac{\vec{d}\cdot\vec{N}_p}{2A^\tau}, \quad p = i, j, k \tag{15}$$

where $A_i = A_{o'jk}$, $A_j = A_{io'k}$ and $A_k = A_{ijo'}$. Note that $\vec{N}_{ijk}$ are the scaled inward normals [18].

Proof Consider Fig. 5, assume $\vec{d}$ is a vector. And, point o is the geometrical center of the triangle ijk; hence, the summation of dark and light shaded domains will be $\frac{1}{3}A^\tau$. Based on the weighted idea,

$$\frac{A_i}{A^\tau} = \frac{A_{jko} - A_{joko'}}{A^\tau} = \frac{1}{3} - \frac{A_{joko'}}{A^\tau} \tag{16}$$

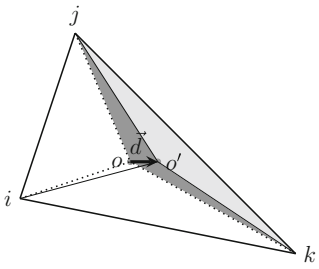

Fig. 5 Determining the area ratios for an arbitrary $\vec{d}$

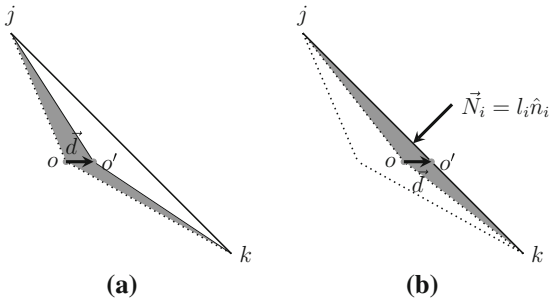

Fig. 6 Moving the OO' in order to find $A_{OBO'C}$. **a** Before moving OO', **b** after moving OO'

By moving the oo' assuming its alignment remains the same, the $A_{joko'}$ will be constant because the perpendicular distance of the points j and k from oo' is the same. Therefore, the oo' is moved along its direction until point o' intersects with jk. Note that $l_i = \bar{jk}$. The dot product of $\hat{n}_A$ and $\vec{d}$ will provide the height of the ojk in Fig. 6b. Therefore,

$$A_{joko'} = -\frac{1}{2}\left(\hat{n}_i \cdot \vec{d}\right) l_i = -\frac{1}{2}\vec{d} \cdot \vec{N}_i \tag{17}$$

Adding to the Eq. 16,

$$\frac{A_i}{A^\tau} = \frac{1}{3} - \frac{A_{joko'}}{A^\tau} = \frac{1}{3} - \frac{1}{A^\tau}\left(-\frac{1}{2}\vec{d} \cdot \vec{N}_i\right) = \frac{1}{3} + \frac{\vec{d} \cdot \vec{N}_i}{2A^\tau} \tag{18}$$

□

Lemma 3.2 *Consider an inward vector $\vec{D}$ starting from a geometrical center of a triangle and ends exactly on the edge i as shown in* Fig. 7. *The area ratios could be written as,*

$$\begin{cases} \frac{A_i}{A^\tau} = \frac{1}{3} - \frac{\vec{N}_i \cdot \vec{N}_i}{3\min\left(\vec{N}_i \cdot \vec{N}_p\right)} \\ \frac{A_j}{A^\tau} = \frac{1}{3} - \frac{\vec{N}_i \cdot \vec{N}_j}{3\min\left(\vec{N}_i \cdot \vec{N}_p\right)} \\ \frac{A_k}{A^\tau} = \frac{1}{3} - \frac{\vec{N}_i \cdot \vec{N}_k}{3\min\left(\vec{N}_i \cdot \vec{N}_p\right)} \end{cases}, \quad p = i, j, k \tag{19}$$

where the $\vec{N}_{ijk}$ are the scaled inward normals.

Proof Since $\vec{D}$ is in the same direction of inward normal, assume

$$\vec{D} = S\vec{N}_i, \quad S > 0 \tag{20}$$

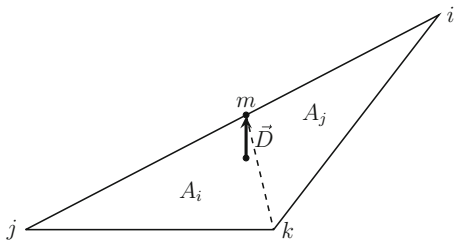

Fig. 7 Determining the area ratios for an inward normal $\vec{D}$ which ends on the edge in front ($A_k = 0$). m is the intersection point

where S is a positive scalar value which make the $\vec{D}$ ends on point m. Based on Eq. 18,

$$\begin{cases} \frac{A_i}{A^\tau} = \frac{1}{3} + \frac{\vec{D}\cdot\vec{N}_i}{2A^\tau} = \frac{1}{3} + \frac{S\vec{N}_i\cdot\vec{N}_i}{2A^\tau} \\ \frac{A_j}{A^\tau} = \frac{1}{3} + \frac{\vec{D}\cdot\vec{N}_j}{2A^\tau} = \frac{1}{3} + \frac{S\vec{N}_i\cdot\vec{N}_j}{2A^\tau} \\ \frac{A_k}{A^\tau} = \frac{1}{3} + \frac{\vec{D}\cdot\vec{N}_k}{2A^\tau} = \frac{1}{3} + \frac{S\vec{N}_i\cdot\vec{N}_k}{2A^\tau} \end{cases} \tag{21}$$

Because the endpoint of $\vec{D}$ is on one of the edges, at least one of the area ratios should be zero. Therefore,

$$\begin{cases} \frac{A_i}{A^\tau} = 0 \\ \text{or} \quad \frac{A_j}{A^\tau} = 0 \\ \text{or} \quad \frac{A_k}{A^\tau} = 0 \end{cases} \quad \Rightarrow \quad S = \frac{-2A^\tau}{3\min\left(\vec{N}_i\cdot\vec{N}_p\right)}, \quad p = i, j, k \tag{22}$$

Since $\min\left(\vec{N}_i\cdot\vec{N}_p\right)$ is always negative therefore, S will be positive. Substituting S into the area ratio equations we get the following equations.

$$\begin{cases} \frac{A_i}{A^\tau} = \frac{1}{3} - \frac{\vec{N}_i\cdot\vec{N}_i}{3\min\left(\vec{N}_i\cdot\vec{N}_p\right)} \\ \frac{A_j}{A^\tau} = \frac{1}{3} - \frac{\vec{N}_i\cdot\vec{N}_j}{3\min\left(\vec{N}_i\cdot\vec{N}_p\right)} \\ \frac{A_k}{A^\tau} = \frac{1}{3} - \frac{\vec{N}_i\cdot\vec{N}_k}{3\min\left(\vec{N}_i\cdot\vec{N}_p\right)} \end{cases}, \quad p = i, j, k \tag{23}$$

□

All the geometrical analysis is required to determine weights w. Despite the tedious mathematical procedures, the general formulation of the weighted approach could be written in a simple and similar form like the Lax–Wendroff method.

$$w_{i\,(\text{point of intreset})}^{e\,(\text{edge number})} = \frac{1}{3} - \frac{\vec{N}_e\cdot\vec{N}_i}{3\min\left(\vec{N}_e\cdot\vec{N}_p\right)}, \quad p = i, j, k \tag{24}$$

Note that we have simplified the notation. It should be mentioned that the summation of w for a specific edge number e will be always one and at least one of the w values should be zero ("Showing Zero Weight For One Characteristic Projection" section of "Appendix 5".). It should be mentioned that e is the repeated index and details will be presented in the next section.

3.3 Weighted LDA

We shall now implement the weighted approach shown in Eq. 24 to the LDA method. We could also apply it to other methods such the SUPG approach but will not do so herein. We shall define the new LDA method as the weighted-LDA approach.

$$\phi_i^\tau = \beta_i^W \phi_T^\tau \tag{25}$$

where,

$$\beta_i^W = \sum_e w_i^e \beta_e, \quad e = i, j, k \tag{26}$$

and,

$$w_i^e = \left(\frac{A_i}{A^\tau}\right)_{\text{edge:}e} = \frac{1}{3} - \frac{\vec{N}_e \cdot \vec{N}_i}{3 \min\left(\vec{N}_e \cdot \vec{N}_p\right)}, \quad p = i, j, k \tag{27}$$

Note that β_e is calculated from the classic LDA.

Lemma 3.3 *The classic 1-target element in classic LDA might become 2-target in the weighted LDA in skewed grid.*

Proof Based on Fig. 2a, if the element is not isosceles ($ik \neq kj$) element then the intersection of $\vec{\lambda}_k^+$ extension with ik or jk will not be at the point k. Therefore, the residual is going to two points (Fig. 2b). □

Lemma 3.4 *The classic 2-target element in classic LDA might become 3-target in the weighted LDA in skewed grid.*

Proof Based on Fig. 3, if the element is not equilateral ($ik \neq kj \neq kj$) element then the intersection of $\vec{\lambda}_i^+$ extension with ik or ji will not be at the point i and, the same is applied for the $\vec{\lambda}_j^+$. Therefore, the residual might be going to three points (Fig. 4). □

Lemma 3.5 *The weighted LDA approach for scalar equation is conservative.*

Proof According to Eq. 25,

$$\begin{aligned}
\phi_i^\tau + \phi_j^\tau + \phi_k^\tau &= \left(\sum_e \left(\tfrac{A_i}{A^\tau}\right)_{\text{edge:}e} \beta_e + \sum_e \left(\tfrac{A_j}{A^\tau}\right)_{\text{edge:}e} \beta_e \right. \\
&\quad \left. + \sum_e \left(\tfrac{A_k}{A^\tau}\right)_{\text{edge:}e} \beta_e \right) \phi_T^\tau \\
&= \left(\sum_e \underbrace{\left(\frac{A_i + A_j + A_k}{A^\tau}\right)_{\text{edge:}e}}_{1} \beta_e \right) \phi_T^\tau \\
&= \underbrace{\left(\sum_e \beta_e\right)}_{1} \phi_T^\tau = \phi_T^\tau
\end{aligned} \tag{28}$$

Hence, conservation is achieved. □

Lemma 3.6 *The weighted LDA approach is LP (Linearity Preserving) for the scalar equations.*

Proof The signals of weighted LDA are,

$$\begin{cases} \phi_i^\tau = \beta_i^W \phi_T^\tau \\ \phi_j^\tau = \beta_j^W \phi_T^\tau \\ \phi_k^\tau = \beta_k^W \phi_T^\tau \end{cases} \quad \wedge \quad \phi_T^\tau \to 0 \quad \Rightarrow \quad \begin{cases} \phi_i^\tau \to 0 \\ \phi_j^\tau \to 0 \\ \phi_k^\tau \to 0 \end{cases} \tag{29}$$

Note that $\beta^{W}_{i,j,k} > 0$. Thus, the LP is satisfied. It will be shown in the next section that the weighted LDA retains second order accuracy (Eq. 40) based on truncation error (TE) analysis. □

3.4 Weighted Blended Approach

Based on [19–21], a blended approach is used to circumvent Godunov's theorem. Because of the fact that the weighted N-scheme is not positive ("Appendix 3"), we shall use the classic N-scheme as the first order of the blending approach. For the second order, the classic and weighted LDA will be used. The original formulation is given by,

$$\phi_i^{\mathrm{B}} = \theta\phi_i^{\mathrm{N}} + (1-\theta)\,\phi_i^{\mathrm{LDA}}, \quad \theta = \frac{|\phi_T|}{\sum_p \left|\phi_p^{\mathrm{N}}\right|} \tag{30}$$

In order to make the blending approach consistent, the averaging in N should be implemented in a way that the total residual for one specific cell should be same as the total residual for the LDA.

4 Truncation Error Analysis for the Linear Case

Although the Taylor series expansion may not be best suited to analyze errors on unstructured anisotropic grids, but we shall use it to perform an analytical error to study the numerical methods on uniform (isotropic) grids. The grid skewness on isotropic grids is controlled by varying the height (h) and width (k) of the element in-which $k = hs$. The s is the stretching parameter to control the skewness (details are in "Appendix 5"). By doing so, we could now perform an analytical truncation error analysis on skewed isotropic grids to provide initial insights of the performance of various numerical methods.

In the truncation error analysis, only the isotropic grids are considered for the reasons mentioned before. The procedure of calculating the general equation are performed based on the main point u_0 which more details could be found in [12]. Thus,

$$\mathrm{TE} = w_0 u_0 + \sum_j w_j u_j \tag{31}$$

where j stands for neighboring points. For an isotropic grid, there are two grid types as shown in Fig. 8. In order to make the calculation easier these two are combined and all the Taylor series analysis will be based on the main point (0) including the calculation for point 1. For instance, in the N-scheme all of the signals which are going to the main point from the neighboring cells is shown in the following.

$$\phi_0^{\tau} = \phi_i^{\tau} + \phi_{ii}^{\tau} + \phi_{iii}^{\tau} + \phi_{iv}^{\tau} + \phi_v^{\tau} + \phi_{vi}^{\tau} + \phi_{vii}^{\tau} + \phi_{viii}^{\tau} \tag{32}$$

Consider $\frac{b}{a} < \frac{k}{h}$; therefore,

$$\phi_i^{\tau} = \phi_{ii}^{\tau} = \phi_{iii}^{\tau} = \phi_{viii}^{\tau} = 0, \tag{33}$$

and,

$$\begin{aligned} \phi_{iv}^{\tau} &= \tfrac{ak}{2}(u_0 - u_5), \quad \phi_v^{\tau} = \tfrac{1}{2}(ak(u_0 - u_5) + bh(u_5 - u_6)), \\ \phi_{vi}^{\tau} &= \tfrac{bh}{2}(u_0 - u_6), \quad \phi_{vii}^{\tau} = \tfrac{bh}{2}(u_0 - u_7), \end{aligned} \tag{34}$$

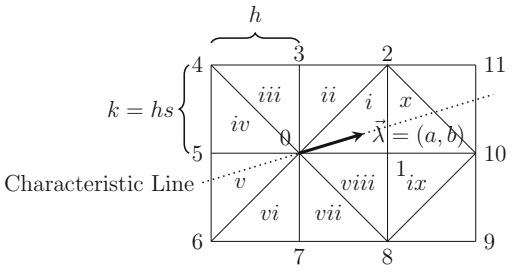

Fig. 8 The isotropic grid points and cell numbers. The s is the ratio of k/h. The $\vec{\lambda}$ is the characteristic vector

Table 1 Normal distance of the neighbor points from the characteristic going through main point for isotropic grid

Point	Distance
1	$-\frac{bh}{r}$
2	$\frac{ak-bh}{r}$
3	$\frac{ak}{r}$
4	$\frac{ak+bh}{r}$
5	$\frac{bh}{r}$
6	$-\frac{ak-bh}{r}$
7	$-\frac{ak}{r}$
8	$-\frac{ak+bh}{r}$
9	$\frac{-ak-2bh}{r}$
10	$-\frac{2bh}{r}$
11	$\frac{ak-2bh}{r}$

thus,

$$\phi_0^\tau = ak(u_0 - u_5) + \frac{bh}{2}(2u_0 + u_5 - 2u_6 - u_7). \tag{35}$$

And for the point 1,

$$\phi_1^\tau = \phi_i^\tau + \phi_{viii}^\tau + \phi_{ix}^\tau + \phi_x^\tau \tag{36}$$

where,

$$\begin{aligned} &\phi_{ix}^\tau = \phi_x^\tau = 0, \quad \phi_i^\tau = \tfrac{1}{2}(bh - ak)(u_0 - u_1), \\ &\phi_{viii}^\tau = \tfrac{1}{2}(ak(-u_0 + u_1) + bh(u_1 - u_8)), \end{aligned} \tag{37}$$

therefore,

$$\phi_1^\tau = \frac{1}{2}(2ak(-u_0 + u_1) + bh(u_0 - u_8)). \tag{38}$$

By combining ϕ_0^τ and ϕ_1^τ the general equation (total truncation error) for classic N-scheme will be,

$$\mathrm{TE} = \frac{\phi_0^\tau + \phi_1^\tau}{2hk} = \frac{2ak(u_1 - u_5) + bh(3u_0 + u_5 - 2u_6 - u_7 - u_8)}{4hk} \tag{39}$$

The normal distance of the streamline with each point will be used to construct the Taylor series (Table 1). All the coefficients for the isotropic grid are demonstrated in Tables 2 and 3.

Table 2 The coefficients of first order methods in general equation for isotropic grid

Method	FV 1^{st}	LxF	N
w_0	$\frac{a}{2h}$	$\frac{a}{h}+\frac{7b}{12hs}$	$\frac{b}{4hs}$
w_1	$\frac{a}{2h}$	$\frac{8as+3b}{12hs}$	$\frac{as+b}{2hs}$
w_2	$\frac{2b-as}{12hs}$	$\frac{2b-3as}{12hs}$	0
w_3	$\frac{2b-as}{12hs}$	$\frac{b-2as}{12hs}$	0
w_4	$\frac{b-as}{6hs}$	$-\frac{3as+b}{12hs}$	0
w_5	$-\frac{a}{3h}$	$-\frac{4as+b}{12hs}$	$\frac{b-2as}{4hs}$
w_6	$-\frac{as+b}{6hs}$	$-\frac{3as+b}{12hs}$	0
w_7	$-\frac{as+2b}{12hs}$	$-\frac{2as+3b}{12hs}$	$-\frac{3b}{4hs}$
w_8	$-\frac{as+2b}{12hs}$	$-\frac{as+2b}{4hs}$	$-\frac{b}{4hs}$
w_9	0	0	0
w_{10}	0	$-\frac{b}{12hs}$	0
w_{11}	0	0	0

Table 3 The coefficients of second order methods in general equation for isotropic grid

Method	FV 2nd	LDA	LDA(W)	L × W
w_0	$\frac{17a}{72h}$	$\frac{3ab^2s+b^3}{4a^2hs^3+4abhs^2}$	$\frac{-2a^3s^3-a^2bs^2+ab^2s\left(3s^2+2\right)+b^3\left(s^2+1\right)}{12ahs^4(as+b)}$	$\frac{2a^3s^3-a^2bs^2+15ab^2s+6b^3}{24a^2hs^3+24abhs^2}$
w_1	$\frac{73a}{144h}$	$\frac{2a^2s^2-abs+b^2}{4ahs^2}$	$\frac{2a^2s^2\left(2s^2+1\right)-abs\left(s^2+1\right)+b^2\left(s^2+1\right)}{12ahs^4}$	$\frac{10a^2s^2-3abs+6b^2}{24ahs^2}$
w_2	$\frac{140b-29as}{432hs}$	$\frac{b(as-b)}{4ahs^2}$	$\frac{a^2s^4+ab\left(2s^3+s\right)-b^2\left(s^2+1\right)}{12ahs^4}$	$\frac{2a^2-\frac{3b^2}{s^2}}{24ah}$
w_3	$\frac{106b-43as}{432hs}$	0	$-\frac{as-2bs^2+b}{12hs^3}$	$\frac{b(4as-3b)}{24ahs^2}$
w_4	$\frac{86b-79as}{432hs}$	$\frac{ab}{4ahs+4bh}$	$\frac{a^2\left(s-s^3\right)+ab\left(s^2+1\right)+b^2s}{12hs^2(as+b)}$	$\frac{-a^2s^2+3abs+b^2}{12ahs^2+12bhs}$
w_5	$-\frac{83a}{216h}$	$\frac{b-2as}{4hs}$	$\frac{b-4as}{12hs}$	$\frac{3b-10as}{24hs}$
w_6	$-\frac{79as+86b}{432hs}$	$-\frac{b}{2hs}$	$-\frac{a\left(s^2-1\right)s+3bs^2+b}{12hs^3}$	$-\frac{as+4b}{12hs}$
w_7	$-\frac{43as+106b}{432hs}$	$-\frac{b^2}{4ahs^2}$	$-\frac{a^2s^2+2abs\left(s^2-1\right)+b^2\left(s^2+1\right)}{12ahs^4}$	$-\frac{b(4as+3b)}{24ahs^2}$
w_8	$-\frac{29as+140b}{432hs}$	$-\frac{b^2}{4ahs^2+4bhs}$	$-\frac{-a^2s^4+abs+b^2\left(2s^2+1\right)}{12hs^3(as+b)}$	$\frac{2a^3s^3+2a^2bs^2-9ab^2s-3b^3}{24ahs^2(as+b)}$
w_9	$\frac{as+2b}{432hs}$	0	0	0
w_{10}	$\frac{31a}{432h}$	0	0	$\frac{3b-2as}{24hs}$
w_{11}	$\frac{as-2b}{432hs}$	0	0	0

Note that for the FV 2nd, the coefficients are not all included since the neighboring points of these 11 nodes also are required

Moreover, the stencil (dependency of points) of each method is shown in Fig. 9. As it can be seen, the domain of dependency for RD methods are more compact relative to the finite volume leading to an early hypothesis that the RD methods are perhaps less sensitive to grid skewness. To find the truncation error, the first step is to expand the neighboring values based on the main point using Taylor series. Note that the solution is constant along the streamline direction. Thus, the Taylor series should expand only in the normal direction to the streamline. The normal distance of the streamline with each point will be used to construct the Taylor series (Table 1). Consequently, for different methods the global truncation error equation will be provided in Eq. 40. The Lax–Friedrich RD approach of [22] will also be included.

The weighted LDA method has a slightly larger computational stencil compared to the original LDA due to the nature of its signals distribution as shown in Fig. 9 but still has much smaller stencil relative to the second order finite volume approach. This is a small sacrifice to be made to model a more physical wave propagation on skewed grids.

Although the spatial order-of-accuracy of the LDA, Lax–Wendroff and weighted LDA are formally second order accurate but each has different coefficients multiplied to the error terms. We shall demonstrate that this terms would affect the performance of the methods on skewed triangular grids.

$$
\begin{aligned}
\mathrm{TE_N} &= \left(\tfrac{b(b-2as)(as+b)}{4r^2s}\right) hu_{nn} + \left(\tfrac{ab(as+b)(4as-b)}{24r^3}\right) h^2 u_{nnn} + O\left(h^3\right)\\
\mathrm{TE_{LxF}} &= \left(-\tfrac{2a^3s^3+a^2bs^2+3ab^2s+b^3}{3r^2s}\right) hu_{nn} + \left(\tfrac{b(2as+b)(a^2s^2+b^2)}{12r^3s}\right) h^2 u_{nnn} + O\left(h^3\right)\\
\mathrm{TE_{LDA}} &= \left(\tfrac{b\left(4a^3s^3-6a^2bs^2+11ab^2s-3b^3\right)}{24r^3s}\right) h^2 u_{nnn}\\
&\quad + \left(\tfrac{b^2(b-2as)(b-as)(as+b)}{48r^4s}\right) h^3 u_{nnnn} + O\left(h^4\right)\\
\mathrm{TE_{FV}}(1^{st}) &= \left(-\tfrac{a\left(2a^2s^2+b^2\right)}{6r^2}\right) hu_{nn} + \left(\tfrac{a^3bs^2+2ab^3}{12r^3}\right) h^2 u_{nnn} + O(h^3)\\
\mathrm{TE_{FV}}(2nd) &= \left(-\tfrac{a^3bs^2+8ab^3}{72r^3}\right) h^2 u_{nnn} + \left(\tfrac{36a^5s^4+77a^3b^2s^2+22ab^4}{432r^4}\right) h^3 u_{nnnn} + O\left(h^4\right)\\
\mathrm{TE_{LDA(W)}} &= \left(\tfrac{ab\left(2a^2+5b^2\right)}{24r^3} - \tfrac{b^4}{24r^3s^3} + \tfrac{ab^3}{6r^3s^2} + \tfrac{-a^2b^2-b^4}{24r^3s} - \tfrac{a^2b^2s}{12r^3}\right) h^2 u_{nnn}\\
&\quad + \left(\tfrac{ab^2\left(3a^2-2b^2\right)}{144r^4} - \tfrac{ab^4}{48r^4s^2} + \tfrac{b^5}{144r^4s^3} + \tfrac{a^3b^2s^2}{72r^4} - \tfrac{a^2b^3s}{144r^4} + \tfrac{b^5-a^2b^3}{144r^4s}\right) h^3 u_{nnnn}\\
&\quad + O\left(h^4\right)\\
\mathrm{TE_{LxW}} &= \left(-\tfrac{b^3(b-3as)}{8r^3s}\right) h^2 u_{nnn} + \left(\tfrac{b^2(9b-10as)(b-as)(as+b)}{144r^4s}\right) h^3 u_{nnnn} + O\left(h^4\right)
\end{aligned}
\tag{40}
$$

where,

$$r = \sqrt{a^2 + b^2}$$

Note that s is the stretching parameter which is connected to the skewness Q as it was mentioned in Eq. 71. The TE of each method depends on the grid skewness, the characteristic vector and the high order derivatives of the variables. The last two factors are problem dependent but the focus would be on the grid skewness dependency.

4.1 Analytical Case Study

We have selected a specific case study to analyze the truncation error of each method. The exact solution of this case study is given by,

$$u_{\mathrm{E}}(x, y) = -\cos\left(2\pi(bx - ay)\right), \quad a, b > 0 \tag{41}$$

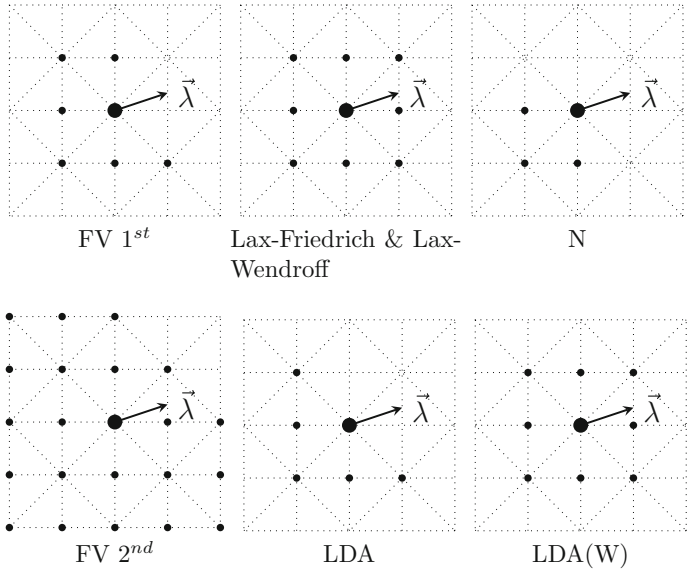

Fig. 9 The stencil for isotropic grid for different methods

In the current test case $a = b = 1$ is chosen. Note that there is more than one possibility for a and b (for instance, for finite volume cell vertex in the isotropic grid it is 24 conditions). For simplicity we just explore one condition. Based on Eq. 40 the truncation error (TE) for the RD and FV methods are shown in Eq. 42.

$$
\begin{aligned}
\mathrm{TE}_{\mathrm{FV}(1^{st})} &= h\left(-\tfrac{2s^2+1}{12}\right)u_{nn} + h^2\left(\tfrac{s^2+2}{24\sqrt{2}}\right)u_{nnn} + O\left(h^3\right)\\
\mathrm{TE}_{\mathrm{LxF}} &= h\left(-\tfrac{\left(s\left(2s^2+s+3\right)+1\right)}{6s}\right)u_{nn} + h^2\left(\tfrac{(2s+1)\left(s^2+1\right)}{24\sqrt{2}s}\right)u_{nnn} + O\left(h^3\right)\\
\mathrm{TE}_{\mathrm{N}} &= h\left(-\tfrac{\left(2s^2+s-1\right)}{8s}\right)u_{nn} + h^2\left(\tfrac{(s+1)(4s-1)}{48\sqrt{2}}\right)u_{nnn} + O\left(h^3\right)\\
\mathrm{TE}_{\mathrm{FV}(2nd)} &= h^2\left(\tfrac{s^2+8}{144\sqrt{2}}\right)u_{nnn} + h^3\left(\tfrac{36s^4+71s^2-26}{1728}\right)u_{nnnn} + O\left(h^4\right)\\
\mathrm{TE}_{\mathrm{LDA}} &= h^2\left(\tfrac{s\left(4s^2-6s+11\right)-3}{48\sqrt{2}s}\right)u_{nnn} + h^3\left(\tfrac{(s-1)(s+1)(2s-1)}{192s}\right)u_{nnnn} + O\left(h^4\right)\\
\mathrm{TE}_{\mathrm{LDA(W)}} &= h^2\left(\tfrac{-2s^4+7s^3-2s^2+4s-1}{48\sqrt{2}s^3}\right)u_{nnn}\\
&\quad + h^3\left(\tfrac{(s+1)\left(2s^4-3s^3+4s^2-4s+1\right)}{576s^3}\right)u_{nnnn} + O\left(h^4\right)\\
\mathrm{TE}_{\mathrm{LxW}} &= h^2\left(\tfrac{3s-1}{16\sqrt{2}s}\right)u_{nnn} + h^3\left(\tfrac{(s-1)(s+1)(10s-9)}{576s}\right)u_{nnnn} + O\left(h^4\right)
\end{aligned}
\tag{42}
$$

The truncation error (TE) plots over skewness are demonstrated in Fig. 10. Note that we consider the linear advection case in order to calculate the derivatives inside the truncation error based on test case 4.1. The analytical errors shows that there is a difference between first order methods as we vary the skewness. In addition, the amount of the error is different. The N-scheme is the best (both in terms of magnitude and minimal error increment) followed by the first order finite volume and lastly the Lax Friedrich method. This is expected because of the high amount of diffusion for the Lax Friedrich method. The N-scheme errors grow somewhat

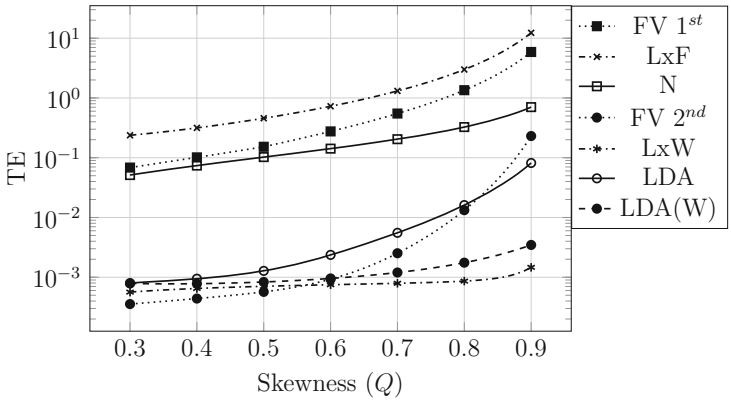

Fig. 10 Truncation error (TE) for linear case with $Q = 0.3 - 0.9$

of linear to the grid skewness whereas the other first order methods have a quadratic rate. This provides another justification to utilize the classic N-scheme for the first order scheme when using the blended approach with weighted LDA.

The analytical results for the second order methods are hugely different as shown in Fig. 10. For the best grid setting, the second order finite volume method produces the least error but the errors rapidly grow as we increase the skewness. The classic and weighted LDA is quite close to each other for the best grid. As the skewness is increased, the difference between TE grows larger but is much less than the second order finite volume. The weighted LDA has an almost a constant error value (or linearly increasing) when the grids are skewed, preserving accuracy even for very large skewness, unlike the original LDA which has a quadratic error increase. This analytically demonstrates that having a more physical signals distribution for a skewed element reduces the dependency on grid changes. The Lax–Wendroff performs similar to the LDA(W).

4.2 Numerical Results for Linear Case

The scalar equation will be solved in a 1×1 area with residual distribution and finite volume methods "Appendix 2" using the same problem presented in the truncation error analysis. The wave is coming from the bottom and left sides of the domain and going out from the top and right sides ($\boldsymbol{\lambda} = a\hat{i} + b\hat{j}$).

The order of accuracy for some of the methods on the best grid ($Q = 0.3$) are depicted in Fig. 11. The numerical L_2 error results are remarkably similar to the analytical TE as shown in Fig. 12 with the highlight of weighted LDA preserving accuracy even for $Q = 0.8$. Note that the weighted LDA preserves second order accuracy for skewed isotropic grids within the range of $Q = 0.3$ until $Q = 0.9$ for this scalar problem, both analytically and numerically but results are omitted for brevity. As in the analytical part, the Lax–Wendroff approach also performs admirably and comparable to the weighted LDA method.

It has to be mentioned that the L_2 error is decreasing in the numerical results. However, in the TE in Fig. 10 shows an error increment or remaining constant. The main reason is coming from the numerical limitations. In the numerical experiments, there would be a grid refinement in one direction (and coarsening in the orthogonal direction) as the grid skewness is increased since the total number of elements is fixed within the domain. This is unavoidable for the grid choice that we use and also not present in the analytical TE analysis. Overall,

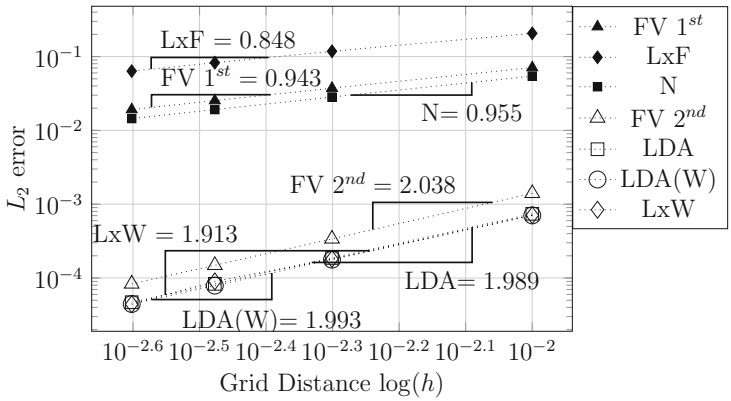

Fig. 11 Numerical L_2 error versus the grid distance in logarithmic scale for the best grid ($Q = 0.3$)

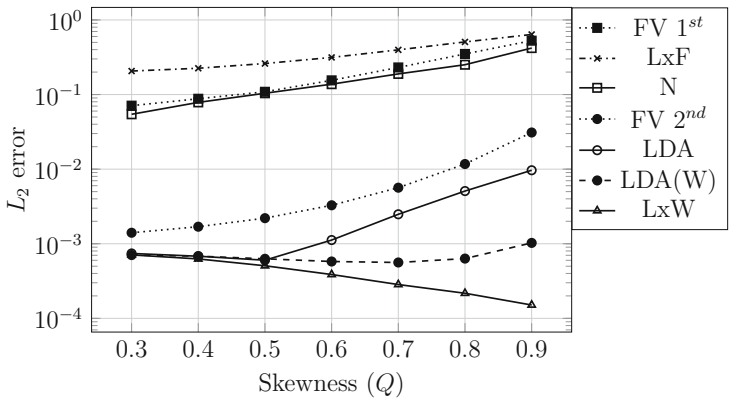

Fig. 12 Numerical L_2 error for linear case with $Q = 0.3 - 0.9$

there would be a downward shift of the error curves for the different methods, relative to the analytical one. Since the weighted LDA and Lax Wendroff methods are pretty much a constant error curve in the analytical part, the downward shifting causes them both to appear to have errors decrease when skewness is increased in the numerical part.

Furthermore, in the Figs. 13, 14 and 15, the error contours are included. As it can be seen, the errors increase as skewness is increased for the first order methods. For the second order methods, the results are almost similar on good grids. As the skewness is increased, the second order FV is the worst followed by the LDA. The weighted LDA demonstrates very little differences in the results when the grids are skewed.

5 Extension of Weighted Approach to the Nonlinear Burgers Equations

Consider the Burgers equation

$$\frac{\partial u}{\partial t} + \vec{\nabla} \cdot \vec{F} = 0, \quad \vec{F} = \frac{u^2}{2}\hat{i} + u\hat{j} \tag{43}$$

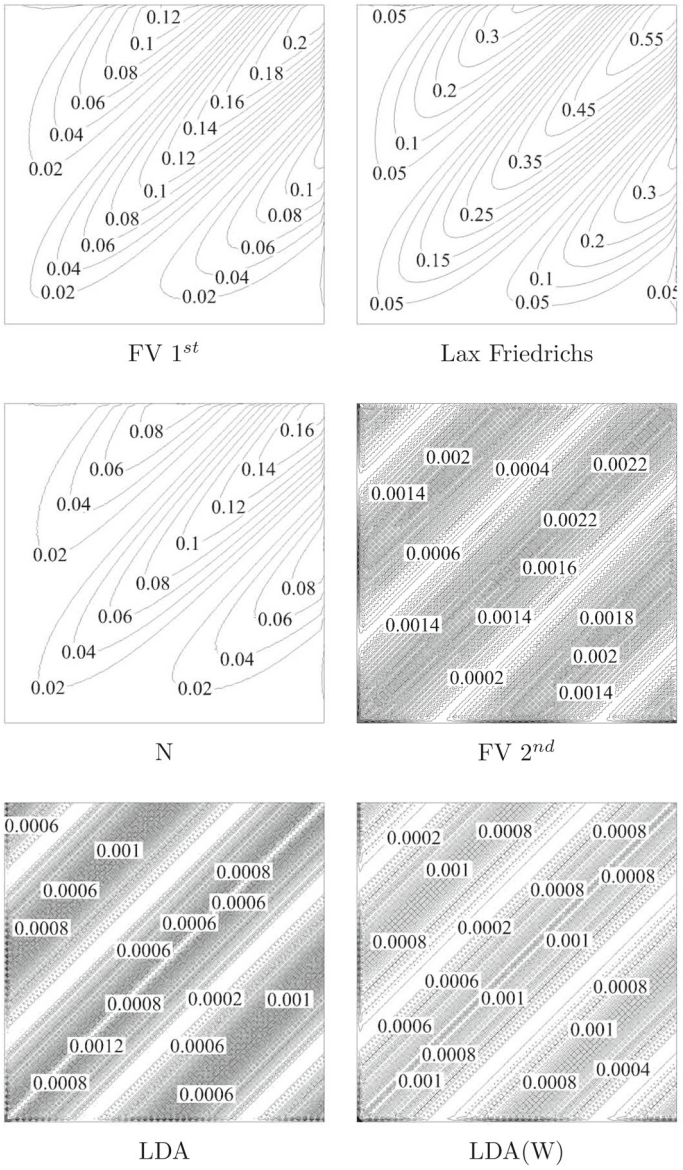

Fig. 13 The error contours on the isotropic grid for $Q = 0.3$

Based on Eq. 1, the characteristic speed is $(a, b) = (u, 1)$. The solution will be solved in a square area $([-1, 0] \times [0, 1])$.

5.1 Nonlinear Burgers Equation

For a nonlinear scalar case, the main idea remains the same. The calculation of signals for weighted LDA has two steps,

- Calculating $\beta_{i,j,k}$ and the total residual from the classic LDA (Eq. 7).

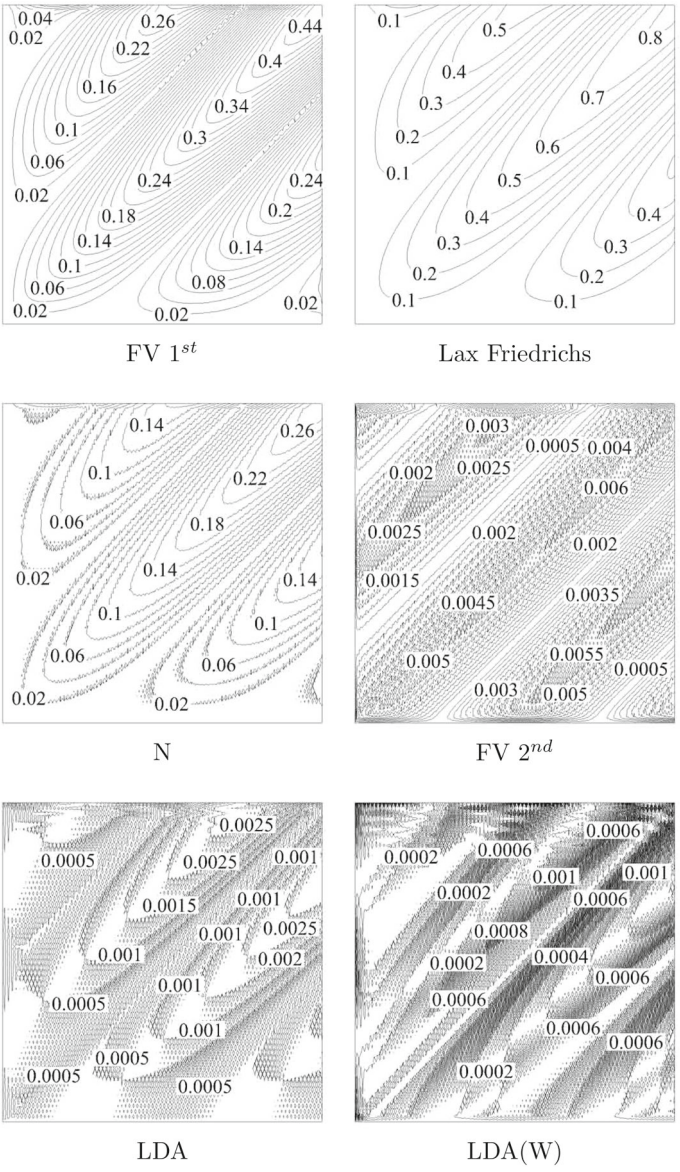

Fig. 14 The error contours on the isotropic grid for $Q = 0.6$

- Determining all the weights from the Eq. 27.
- Use Eq. 25 in order to find weighted LDA signals.

5.2 Numerical Results for Nonlinear Cases

5.2.1 Expansion Wave

For the expansion case, the bottom edge is the inlet wave,

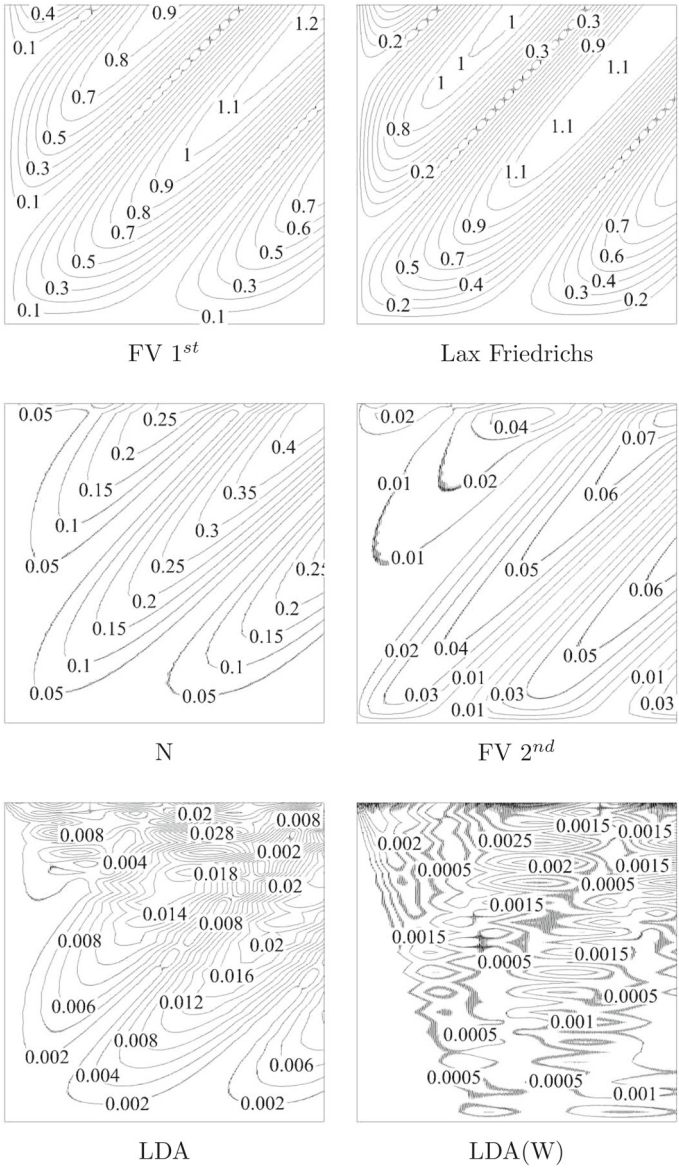

Fig. 15 The error contours on the isotropic grid for $Q = 0.9$

$$u_{\text{bottom}} = \frac{U_r + x(U_r - U_l)}{1 + y(U_r - U_l)}, \quad U_r > U_l \tag{44}$$

where U_r and U_l are the right and left side of the values. The condition $U_r > U_l$ ensures that the solution will expand without any shock waves. In this study, $U_r = 1.5$ and $U_l = -0.5$ are chosen. In order to compare the numerical results, the cross section of $y = 0.5$ are shown for different methods in Figs. 16, 17 and 18.

As demonstrated in Fig. 19, the most accurate and least sensitive method for non linear smooth case is the weighted LDA. The LDA method performs reasonably well on grids with

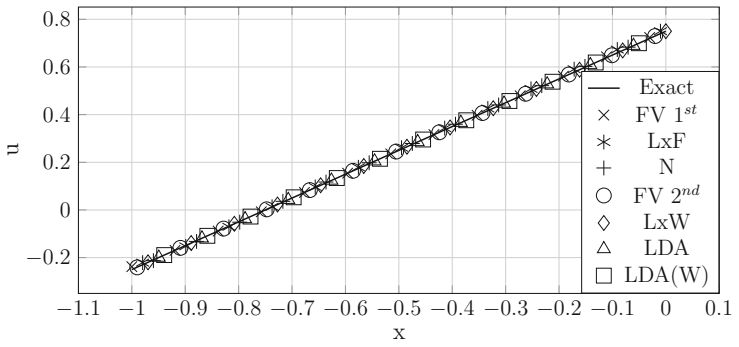

Fig. 16 The cross section profiles for expansion case ($Q = 0.3$)

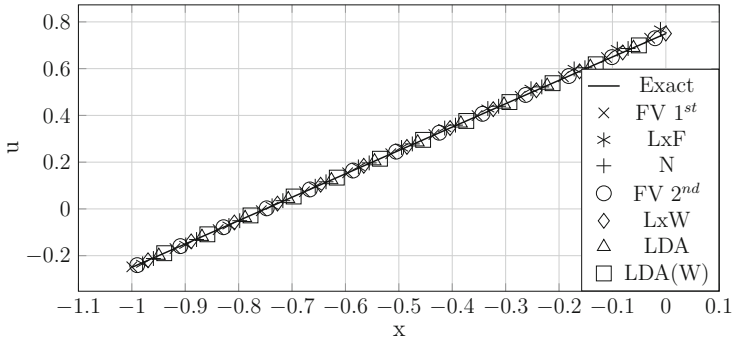

Fig. 17 The cross section profiles for expansion case ($Q = 0.5$)

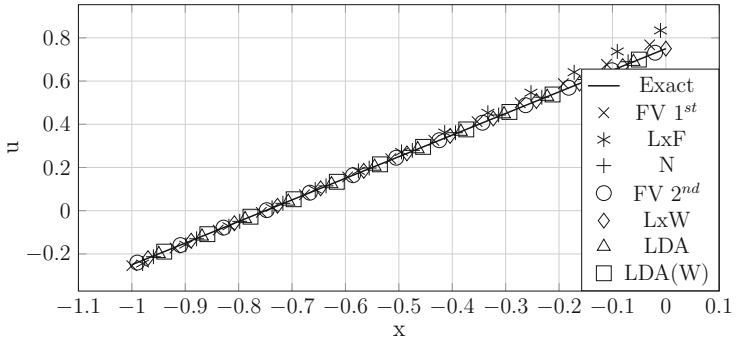

Fig. 18 The cross section profiles for expansion case ($Q = 0.8$)

low skewness. Nonetheless, its L_2 error is increases when skewnesss is increased unlike the weighted LDA. The second order finite volume method is the worst second order method.

The N scheme is the most dependable first order method. The first order finite volume method performs really good on the best grids but rapidly deteriorates as grid skewness is increase. Moreover, the Lax–Friedrichs method is the worst. Like the second order finite volume, the first order version is also showing the most grid-dependent result and even more than the Lax Friedrichs RD method.

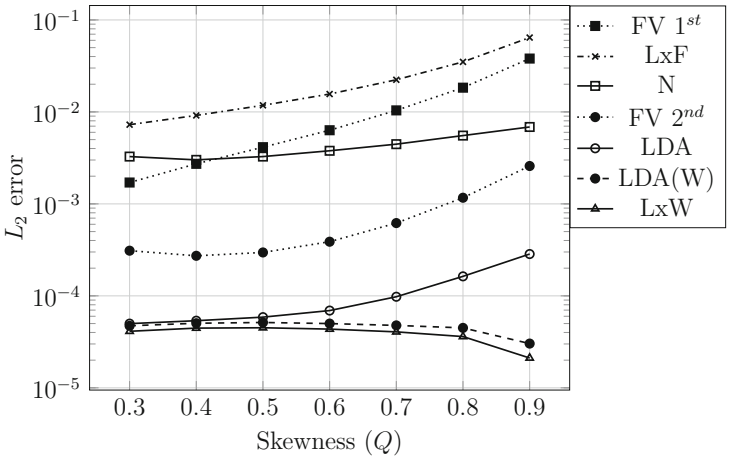

Fig. 19 Numerical L_2 error for non-linear expansion case with $Q = 0.3 - 0.9$

5.2.2 Shock-Tree Problem

Recall the Burgers' equation (Eq. 43), with the inflow boundary at the bottom,

$$u(x, 0) = 1.5 - 2x \tag{45}$$

The steady state exact solution is,

$$u(x, y) = \begin{cases} -0.5 & y \leq \frac{1}{2} \quad \& \quad \frac{x-\frac{3}{4}}{y-\frac{1}{2}} < \frac{1}{2} \\ 1.5 & y \leq \frac{1}{2} \quad \& \quad \frac{x-\frac{3}{4}}{y-\frac{1}{2}} > \frac{1}{2} \\ \max\left(-0.5, \min\left(1.5, \frac{x-\frac{3}{4}}{y-\frac{1}{2}}\right)\right) & \text{elsewhere} \end{cases} \tag{46}$$

The initial condition is set to $u = 0$. We represent the solutions computed for the isotropic grid a discussed in section "Appendix 5". Furthermore, the cross sectional results of each method are shown in Figs. 20, 21 and 22. The contour plots for the best grid is demonstrated in Fig. 24. Note that the Lax–Wendroff and the LDA(W) results are very similar therefore, we only show LDA(W) for the most part.

There is small difference in the results of the second order methods near the shock as the grids are skewed.The weighted LDA produces oscillations around the shock due to Godunov's theorem similar to other second order methods. However, monotone results are achieved once a blended (limited) LDA and blended weighted LDA are being used.

Moreover, the blending and the PSI approaches are tested in order to show the behavior of these methods in Fig. 23. As it can be seen, the blending approaches and the PSI are producing a monotone results.

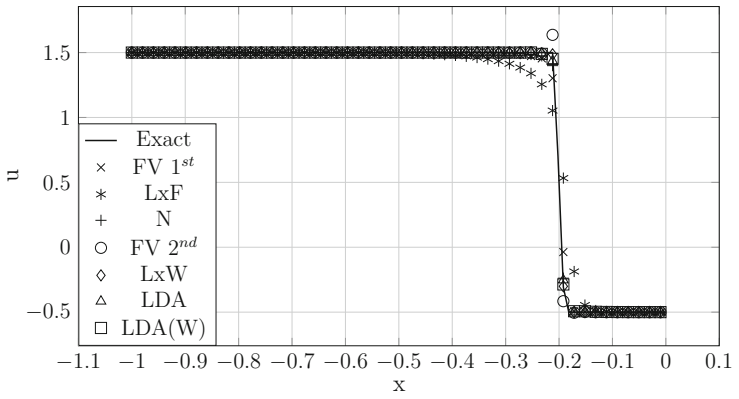

Fig. 20 The cross section profiles for shock-tree case ($Q = 0.3$)

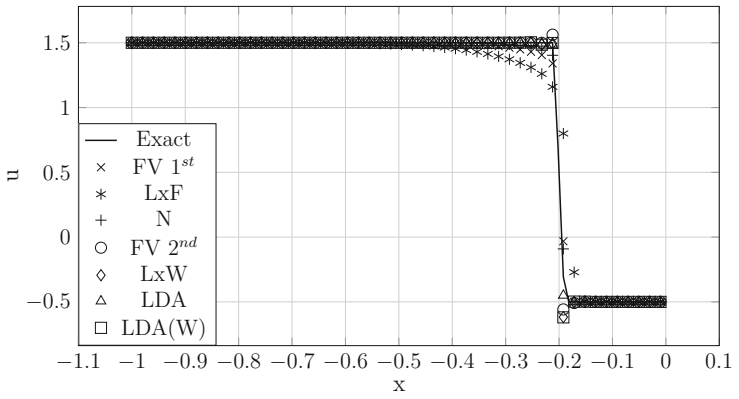

Fig. 21 The cross section profiles for shock-tree case ($Q = 0.5$)

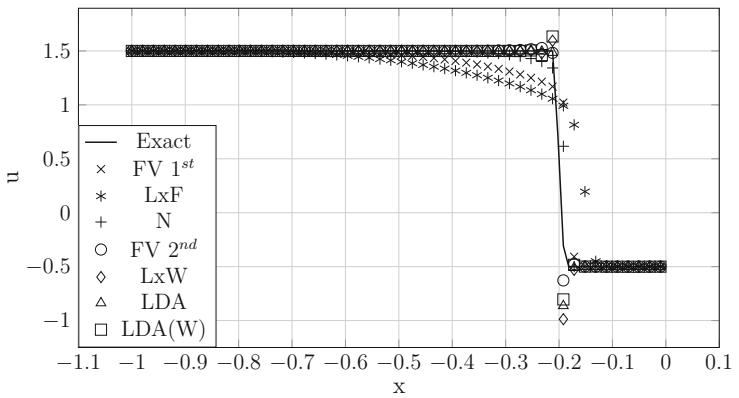

Fig. 22 The cross section profiles for shock-tree case ($Q = 0.8$)

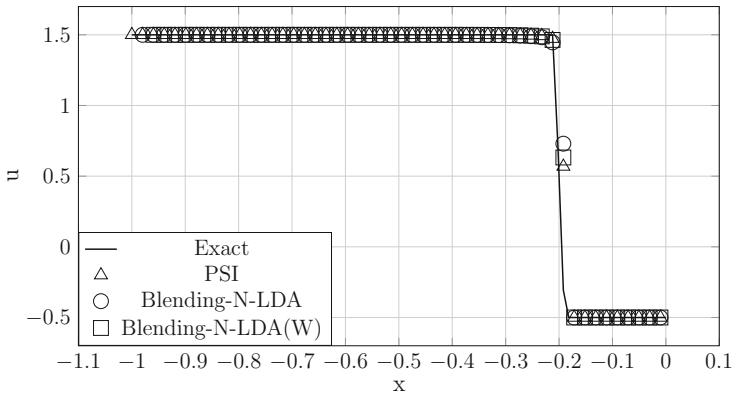

Fig. 23 The cross section profiles for shock-tree case ($Q = 0.8$) for the blended approaches

6 Extension of Weighted Approach to the System of Euler Equations

The system of ideal Euler equations with the conserved variables $\boldsymbol{u} = (\rho, \rho u, \rho v, \rho E)^T$ satisfy the following.

$$\boldsymbol{u}_t + \nabla \cdot \vec{\boldsymbol{F}} = 0 \tag{47}$$

or in integral form

$$\oint (\boldsymbol{u} dA - \vec{\boldsymbol{F}} dt) = 0 \tag{48}$$

with the fluxes defined as $\vec{\boldsymbol{F}} = (\boldsymbol{f}(\boldsymbol{u}), \boldsymbol{g}(\boldsymbol{u}))$.

$$\boldsymbol{f}(\boldsymbol{u}) = \begin{bmatrix} \rho u \\ \rho u^2 + P \\ \rho uv \\ \rho uH \end{bmatrix}, \qquad \boldsymbol{g}(\boldsymbol{u}) = \begin{bmatrix} \rho v \\ \rho uv \\ \rho v^2 + P \\ \rho vH \end{bmatrix} \tag{49}$$

where the total energy and total enthalpy are defined as $E = e + \frac{u^2+v^2}{2}$ and $H = E + \frac{P}{\rho}$. The compatibility relation between pressure and internal energy e is used for closure, $P = \rho e(\gamma - 1)$ and γ is the fluids ratio of specific heats. The Jacobian matrix is defined as the following.

$$J = \boldsymbol{R} \Lambda \boldsymbol{R}^{-1} \tag{50}$$

where the right eigenvectors are written as follows.

$$\boldsymbol{R} = \begin{bmatrix} 1 & 1 & 0 & 1 \\ u - an^x & u & -n^y & u + an^x \\ v - an^y & v & n^x & v + an^y \\ h - aq & \frac{u^2+v^2}{2} & r & h + aq \end{bmatrix} \tag{51}$$

where n^x and n^y is a unique vector that is illustrating the direction of the decomposition. We define, $r = -un^y + vn^x$ and $q = un^x + vn^y$ are the velocity along and normal to the decomposition direction. And,

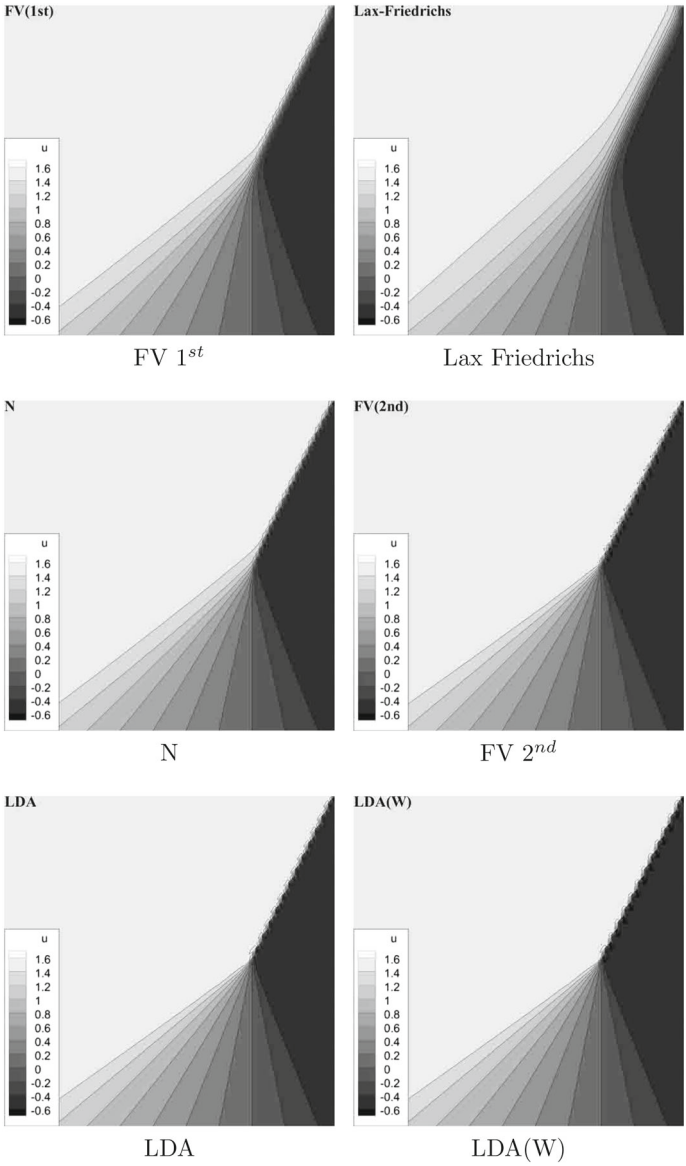

Fig. 24 The contours of the shock tree case on the isotropic grid for $Q = 0.3$

$$\Lambda = \begin{bmatrix} q-a & 0 & 0 & 0 \\ 0 & q & 0 & 0 \\ 0 & 0 & q & 0 \\ 0 & 0 & 0 & q+a \end{bmatrix} \tag{52}$$

where,

$$a = \sqrt{\frac{\gamma P}{\rho}} \tag{53}$$

6.1 Classic LDA

In the classic LDA the signal distribution is,

$$\boldsymbol{\phi}_i = \boldsymbol{\beta}_i \boldsymbol{\phi}_T \tag{54}$$

where,

$$\boldsymbol{\beta}_i = K_i^+ \left(\sum_p K_p^+ \right)^{-1}, \quad p = i, j, k \tag{55}$$

The definition of K_i^+ is,

$$K_i^+ = \frac{1}{2} R_i \left(\vec{\Lambda} \cdot \vec{N} \right)_i^+ L_i \tag{56}$$

where,

$$(c)^+ = \begin{cases} c & c > 0 \\ 0 & c \leq 0 \end{cases} \tag{57}$$

Note that the $\bar{(.)}$ variables are calculated based on the arithmetic average of a cell. $\bar{(.)}_i$ represents the cell average value using a specific edge (i, j, k) inward normal.

6.2 Lax–Wendroff

The Lax–Wendroff for the system of equations discussed in [17] which is given by,

$$\boldsymbol{\phi}_i = \boldsymbol{\beta}_i^{\mathrm{LxW}} \boldsymbol{\phi}_T \tag{58}$$

where,

$$\boldsymbol{\beta}_i^{\mathrm{LxW}} = \frac{1}{3} I + \nu_c K_i \left(\sum_p \left| K_p \right| \right)^{-1}, \quad p = i, j, k \tag{59}$$

The ν_c is the cell CFL number.

6.3 Weighted LDA

6.3.1 Geometrical Aspects on Skewed Grids for System of Equations

In the system of equations the eigenvalues could not be implemented as the scalar since the acoustic waves have omni direction. Instead, another parameter is defined to show the residual portion coming from a specific edge. Consider Eq. (56), the $\left(\vec{\Lambda} \cdot \vec{n} \right)_i^+$ is a scalar quantity. However, it shows the projection of the characteristic vector along the inward normal of an edge. Therefore, one could reconstruct a vector based on

$$\vec{\Lambda}_i^{\vec{n}_i} = \left(\vec{\Lambda} \cdot \vec{n} \right)_i^+ \vec{n}_i \tag{60}$$

If $\left(\vec{\Lambda} \cdot \vec{n} \right)_i$ is positive (negative), the direction of this vector will be inward (outward) normal of the edge.

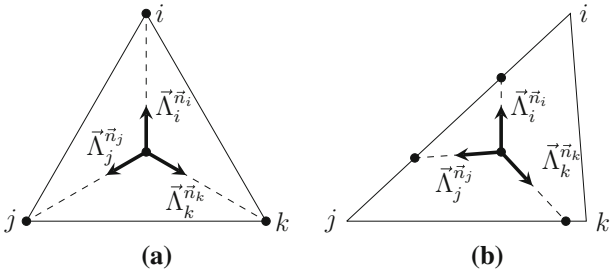

Fig. 25 General signal distribution on two elements. **a** Equilateral element, **b** Skewed element

In the classic approaches, all the residual portion that is coming form positive $\vec{\Lambda}_i^{\vec{n}_i}$ will be going to point i that is suitable for equilateral grids (Fig. 25a). On the other hand, for a skewed grid as it is illustrated in Fig. 25, we are using the weighted idea to distribute the residual. Consequently, even though the RD methods are compact and less sensitive to the grid, the distribution in classic RD approaches could be improved in order to generate a method that is distributing the signals considering. The geometrical aspects here is same as scalar base on the formulation. Nevertheless, the difference is lying in the fact that for system of equations there are three inward normal directions that we have to take into account instead of one single characteristic vector. Recall Eq. 24,

$$w_{i\,(\text{point of interest})}^{e\,(\text{edge number})} = \left(\frac{A_i}{A^\tau}\right)_{\text{edge:}e} = \frac{1}{3} - \frac{\vec{N}_e \cdot \vec{N}_i}{3\min\left(\vec{N}_e \cdot \vec{N}_p\right)}, \quad p = i, j, k \tag{61}$$

where A^τ is the total area of the element.

6.3.2 Formulation

In the Euler system of equations, the formulation of weighted LDA is the same as the scalar Eq. 25 but the signals $\boldsymbol{\phi}_i$ are now vectors. Thus,

$$\boldsymbol{\phi}_i^\tau = \left(\sum_e w_i^e \boldsymbol{\beta}_e\right) \boldsymbol{\phi}_T^\tau, \quad e = i, j, k \tag{62}$$

The $\boldsymbol{\beta}_{i,j,k}$ is determined exactly like the classic LDA in Eq. 55. Note that,

$$w_i^e = \left(\frac{A_i}{A^\tau}\right)_{\text{edge:}e} = \frac{1}{3} - \frac{\vec{N}_e \cdot \vec{N}_i}{3\min\left(\vec{N}_e \cdot \vec{N}_p\right)}, \quad p = i, j, k \tag{63}$$

Lemma 6.1 *The weighted LDA approach for system of equations is conservative.*

Proof The summation of signals is,

$$\begin{aligned}\boldsymbol{\phi}_i^\tau + \boldsymbol{\phi}_j^\tau + \boldsymbol{\phi}_k^\tau &= \left(\sum_e \left(\frac{A_i}{A^\tau}\right)_{\text{edge}:e} \boldsymbol{\beta}_e + \sum_e \left(\frac{A_j}{A^\tau}\right)_{\text{edge}:e} \boldsymbol{\beta}_e \right.\\ &\quad \left. + \sum_e \left(\frac{A_k}{A^\tau}\right)_{\text{edge}:e} \boldsymbol{\beta}_e \right) \boldsymbol{\phi}_T^\tau \\ &= \left(\sum_e \underbrace{\left(\frac{A_i + A_j + A_k}{A^\tau}\right)_{\text{edge}:e}}_{1} \boldsymbol{\beta}_e \right) \boldsymbol{\phi}_T^\tau \\ &= \underbrace{\left(\sum_e \boldsymbol{\beta}_e\right)}_{\boldsymbol{I}} \boldsymbol{\phi}_T^\tau = \boldsymbol{\phi}_T^\tau \end{aligned} \tag{64}$$

Hence, the conservation is satisfied. □

Lemma 6.2 *The weighted LDA approach for system of equations is LP (Linearity Preserving).*

Proof According to Eq. 62,

$$\begin{cases} \boldsymbol{\phi}_i^\tau = \left(\sum_e \left(\frac{A_i}{A^\tau}\right)_{\text{edge}:e} \boldsymbol{\beta}_e\right) \boldsymbol{\phi}_T^\tau \\ \boldsymbol{\phi}_j^\tau = \left(\sum_e \left(\frac{A_j}{A^\tau}\right)_{\text{edge}:e} \boldsymbol{\beta}_e\right) \boldsymbol{\phi}_T^\tau \\ \boldsymbol{\phi}_k^\tau = \left(\sum_e \left(\frac{A_k}{A^\tau}\right)_{\text{edge}:e} \boldsymbol{\beta}_e\right) \boldsymbol{\phi}_T^\tau \end{cases} \quad \wedge \quad \boldsymbol{\phi}_T^\tau \to 0 \quad \Rightarrow \quad \begin{cases} \boldsymbol{\phi}_i^\tau \to 0 \\ \boldsymbol{\phi}_j^\tau \to 0 \\ \boldsymbol{\phi}_k^\tau \to 0 \end{cases} \tag{65}$$

Thus, the LP condition is satisfied. □

The Lax–Wendroff version for the systems of Euler equations can be readily found in [17]. Note that, the weighted LDA is still an upwind-type method unlike the Lax–Wendroff approach since only the positive (upwind) K_i^+ is considered for the signals distribution.

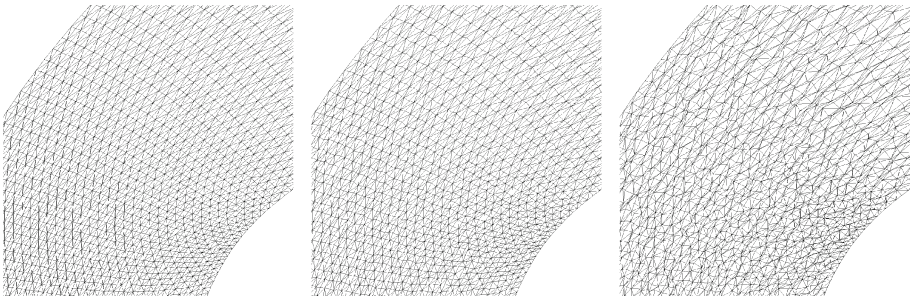

Fig. 26 The RG1, RG2 and RG4 grids

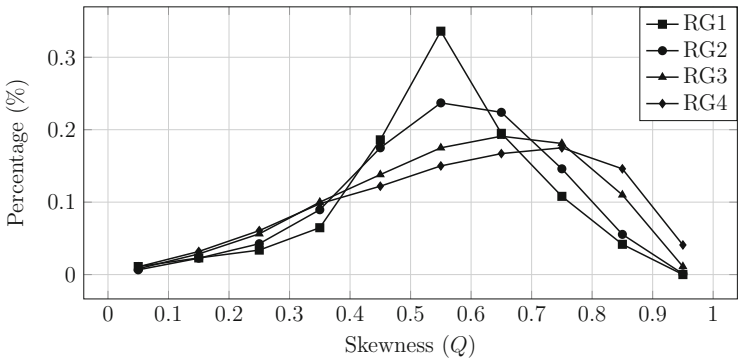

Fig. 27 Histogram for different grid disturbances using in the Ringleb case

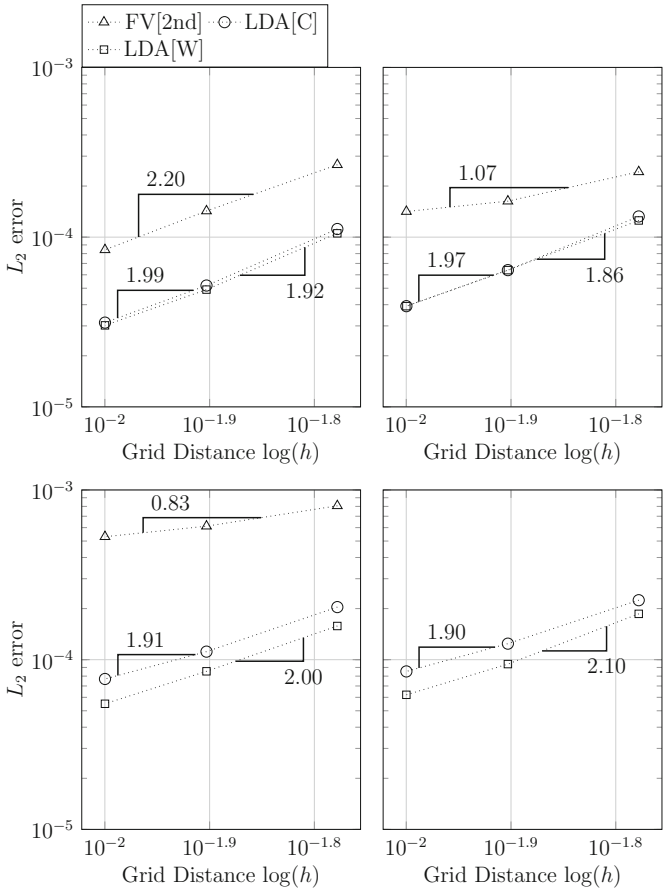

Fig. 28 Numerical L_2 error versus the grid distance in logarithmic scale for different grid types ($RG1$, $RG2$, $RG3$ and $RG4$), respectively

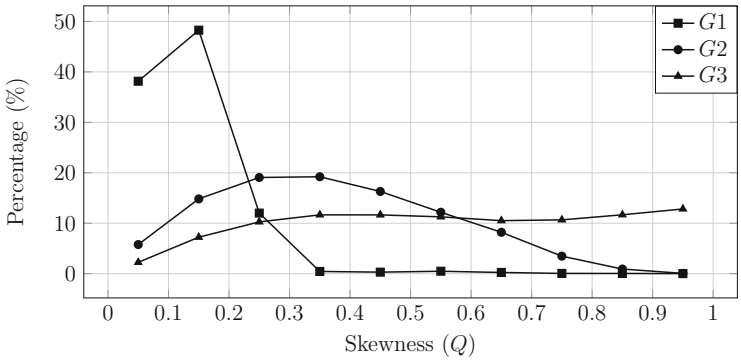

Fig. 29 Histogram for different grid disturbances using in the cylinder case; $G1$, $G2$ and $G3$ which are defined in "Anisotropic Grid" section of "Appendix 5"

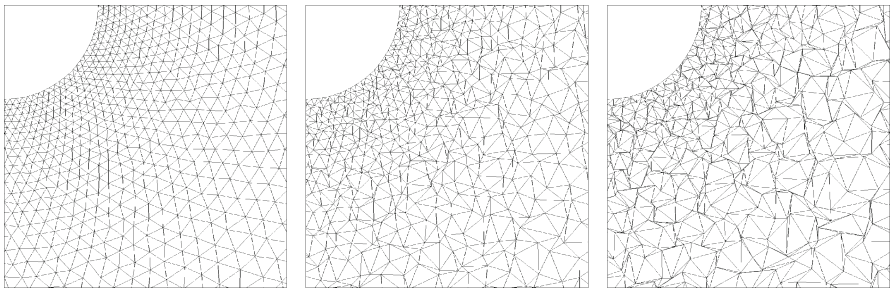

Fig. 30 The $G1$, $G2$ and $G3$ grids

6.4 Numerical Results for System of Euler Equations

6.4.1 Ringleb Flow

The Ringleb flow [23] is used to study the order of accuracy analysis for the Euler equation. In this paper, the order of accuracy of the second order finite volume ("Appendix 2"), classic LDA and weighted LDA are examined with Ringleb flow using different disturbance percentage of the grid (Fig. 26). The distribution of grid skewness for each grid type is demonstrated in Fig. 27. The RG1, RG2 and RG3 are showing the 20, 50 and 90% of disturbances. Moreover, the RG4 stands for the 90% disturbances which is disturbed twice.

The order of accuracy for different methods are demonstrated in Fig. 28. The second order FV shows a dramatic order of accuracy drop. Although it is second order for RG1, it drops significantly to first order in RG2. More importantly, on RG3 grid, the results become erratic in which the order of accuracy can not be measured. Finally, the second order finite volume does not even have a converged solution for RG4. Overall, the LDA and weighted LDA preserve the order of accuracy as the grid becomes highly skewed but the former has a larger increment in error magnitude. This demonstrates that the weighted LDA is less sensitive to grid changes.

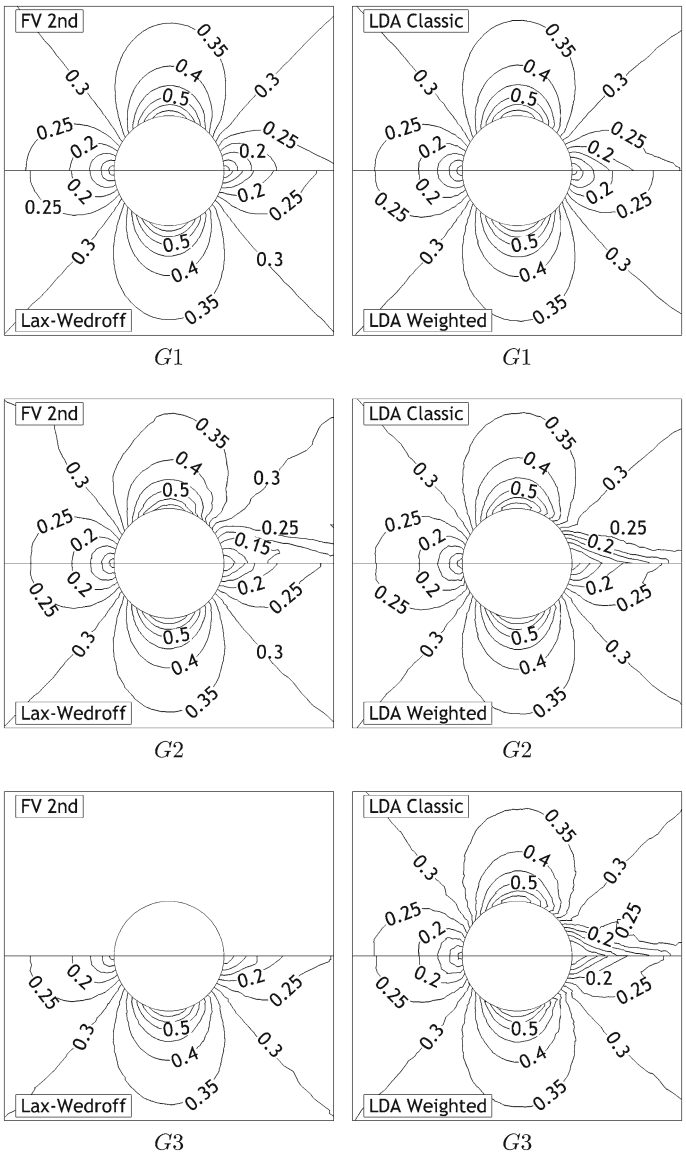

Fig. 31 2nd order finite volume, Lax–Wendroff, classic and weighted LDA for $G1$, $G2$ and $G3$

6.4.2 Subsonic Cylinder

The weighted LDA approach is evaluated on a subsonic flow over cylinder with incoming free stream Mach number 0.3. In order to shed light on the reliability and solidness of the methods, the grid will be disturbed and randomized by three steps which are 20, 50 and 90% ($G1$, $G2$ and $G3$) demonstrated in Figs. 29 and 30.

There are three different grid sets in which the second order methods including 2nd order finite volume ("Appendix 2"), classic and weighted LDA are tested. After disturbing the grid point, the quality of the grid is measured by the percentage of the grid number's skewness.

In Fig. 29, the distribution of the skewness versus the percentage of number of the cells is shown.

All the results are shown in Fig. 31. Clearly, the weighted LDA is much superior to the original LDA and second order finite volume methods particularly in recovering the stagnation point at the back of the cylinder. In fact, the second order finite volume solution diverges for the worst grid set up. It should be mentioned that the two LDA methods are not identical for the best grid since around the cylinder the skewness is not absolutely zero ($Q \sim 0.0197$). The more disturbed the grid, the more the difference between classic and weighted LDA will be. The LDA(W) is very similar to the Lax–Wendroff as the whole concept is similar, except for the fact that the LDA(W) is upwind method and Lax–Wendroff is a central scheme.

7 Conclusion

It is demonstrated in this paper that overall the finite volume methods are more susceptible to results deterioration compared to the residual distribution methods. This is mainly due to perhaps the use of non-compact stencils of the former relative to the latter. Changes in grids skewness will have a much more detrimental effects to the orientation of the numerical methods with non-compact stencils relative to a method with compact stencil.

However, the classic LDA method in this paper is only slightly better relative to second order finite volume method in terms of preserving accuracy. Unlike the original LDA, the new weighted LDA method preserves accuracy for almost all skewness and this is demonstrated for the selected test problems herein using scalar equations and the system of Euler equations. This is due to the weighted LDA not only depends on the local wave-characteristics to distribute the residuals from classic LDA but also actively adjusting based on the grid topology. For an equilateral triangular element, the weighted LDA reduces to the original LDA. However, the process of weight distribution being locally applied on each node will be triggered once the elements deviate from equilateral triangles. This locally-adaptive process will cater for changes in grids even though there is no change in the wave-characteristics. Although the weighted LDA has a larger computational stencil compared to the original LDA but it still remains compact, within one neighboring node to the main node of interest. Nevertheless, the signals formulation of the weighted LDA is relatively simple and has a similar form to the Lax–Wendroff method in a sense that it may lose upwinding properties for highly skewed grid. This is the price to be paid for achieving less sensitivity on grid skewness.

Since the weighted LDA has a larger computational stencil yet remain compact, the prospect of extending to higher order accuracy is more natural compared to classic LDA. Various combination of the weights to each node can be explored to cancel out the low order truncation error terms and the work is currently underway.

Acknowledgements We would like to thank Universiti Sains Malaysia for financially supporting this research work under the University Research Grant (NO: 1001/PAERO/814152) and to Malaysian Ministry of Higher Education Fundamental Research Grant (NO: 203/PAERO/6071316).

Appendix 1: General Equation for First Order Finite Volume

According to Fig. 32, the scaled normal vector for each edge and the upwind first order value for the edge are shown in Table 4. Therefore, the line integration of the first order finite volume will be,

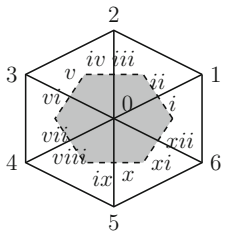

Fig. 32 The isosceles grid topology for two kinds (finite volume cells are *shaded*)

$$\oint \boldsymbol{F}\cdot\hat{n}dS = u_0\left(\tfrac{ak}{2}+\tfrac{bh}{6}+\tfrac{ak}{2}+\tfrac{bh}{3}+\tfrac{bh}{3}+\tfrac{bh}{6}+\tfrac{ak}{2}-\tfrac{bh}{6}+\tfrac{ak}{2}-\tfrac{bh}{6}\right) + u_3\left(-\tfrac{ak}{2}+\tfrac{bh}{6}-\tfrac{ak}{2}+\tfrac{bh}{6}\right)+u_4\left(-ak-\tfrac{bh}{3}\right)+u_5\left(-\tfrac{2bh}{3}\right) \tag{66}$$

Thus,

$$\mathrm{TE} = \frac{3ak(2u_0-u_3-u_4)+bh(2u_0+u_3-u_4-2u_5)}{6hk} \tag{67}$$

Appendix 2: Finite Volume Method Characteristics

The second order finite volume which is used in this paper is based on the following characteristics:

- The node center (cell vertex) is used in order to maintain same computational points as residual distribution approach.
- The gradients are calculated based on Least Square approach for each point [17].
- The solver is also same as the residual distribution to ensure a true comparison. Hence, the first order explicit is used [17].
- The local time step is implemented based on the specific local time step [24].
- The upwind discretization for the scalar equation is constructed by Roe's flux. Also, for the Euler equations in this study we use the Roe's flux [25].

Appendix 3: Lax–Friedrichs

In the Lax–Friedrichs method the sub-residuals should be constructed to ensure the first order accuracy and also L_∞ stability.

$$\phi_i^\tau = \bar{\phi}^\tau + \alpha\left(u_i-\bar{u}\right), \quad \alpha > \max||K_i|| \tag{68}$$

These choices guaranty that the scheme is L_∞ stable [22]. Note that, the $\bar{\phi}^\tau$ and $\bar{u}$ are the arithmetic average of ϕ_i^τ and u_i for a cell.

Table 4 The scaled normal of the cell vertex finite volume cell; and, the upwind edge value ($\frac{b}{a} < \frac{k}{h}$)

Edge	i	ii	iii	iv	v	vi	vii	$viii$	ix	x	xi	xii
N_x	$\frac{k}{2}$	$\frac{k}{2}$	0	0	$-\frac{k}{2}$	$-\frac{k}{2}$	$-\frac{k}{2}$	$-\frac{k}{2}$	0	0	$\frac{k}{2}$	$\frac{k}{2}$
N_y	$\frac{h}{6}$	$\frac{h}{6}$	$\frac{h}{3}$	$\frac{h}{3}$	$\frac{h}{6}$	$\frac{h}{6}$	$-\frac{h}{6}$	$-\frac{h}{6}$	$-\frac{h}{3}$	$-\frac{h}{3}$	$-\frac{h}{6}$	$-\frac{h}{6}$
u_{Edge}	u_0	u_0	u_0	u_0	u_3	u_3	u_4	u_4	u_5	u_5	u_0	u_0

Appendix 4: Non-positivity of Weighted N scheme

Lemma 7.1 *The weighted N-scheme approach does NOT satisfy positivity for a skewed element.*

Proof Using Eq. 25 for the N-scheme to construct weighted N leads us to,

$$\begin{aligned}
\phi_i^{\mathrm{N(W)}} &= \left(\frac{1}{3} - \frac{\vec{N}_i\cdot\vec{N}_i}{3\min\left(\vec{N}_i\cdot\vec{N}_p\right)}\right)\phi_i^{\mathrm{N}} + \left(\frac{1}{3} - \frac{\vec{N}_j\cdot\vec{N}_i}{3\min\left(\vec{N}_j\cdot\vec{N}_p\right)}\right)\phi_j^{\mathrm{N}} \\
&\quad + \left(\frac{1}{3} - \frac{\vec{N}_k\cdot\vec{N}_i}{3\min\left(\vec{N}_k\cdot\vec{N}_p\right)}\right)\phi_k^{\mathrm{N}} \\
\phi_j^{\tau} &= \left(\frac{1}{3} - \frac{\vec{N}_i\cdot\vec{N}_j}{3\min\left(\vec{N}_i\cdot\vec{N}_p\right)}\right)\phi_i^{\mathrm{N}} + \left(\frac{1}{3} - \frac{\vec{N}_j\cdot\vec{N}_j}{3\min\left(\vec{N}_j\cdot\vec{N}_p\right)}\right)\phi_j^{\mathrm{N}} \\
&\quad + \left(\frac{1}{3} - \frac{\vec{N}_k\cdot\vec{N}_j}{3\min\left(\vec{N}_k\cdot\vec{N}_p\right)}\right)\phi_k^{\mathrm{N}} \\
\phi_k^{\tau} &= \left(\frac{1}{3} - \frac{\vec{N}_i\cdot\vec{N}_k}{3\min\left(\vec{N}_i\cdot\vec{N}_p\right)}\right)\phi_i^{\mathrm{N}} + \left(\frac{1}{3} - \frac{\vec{N}_j\cdot\vec{N}_k}{3\min\left(\vec{N}_j\cdot\vec{N}_p\right)}\right)\phi_j^{\mathrm{N}} \\
&\quad + \left(\frac{1}{3} - \frac{\vec{N}_k\cdot\vec{N}_k}{3\min\left(\vec{N}_k\cdot\vec{N}_p\right)}\right)\phi_k^{\mathrm{N}}
\end{aligned} \tag{69}$$

where,

$$\phi_{i,j,k}^{\mathrm{N}} = k_{i,j,k}^{+}(u_{i,j,k} - \hat{u}), \quad \hat{u} = \frac{\sum_p k_p^{-} u_p}{\sum_p k_p^{-}} \tag{70}$$

to satisfy local positivity for a signal (ϕ_i) all the coefficients of the main nodes u_i should be positive and all the coefficients for other points within the same element should be negative. For instance in ϕ_i all the coefficients of u_i must be positive. The other coefficients need to be negative. While, K_j^{+}, K_k^{+} are positive; also, all the values of w are positive; the positivity is lost according to the second and third term. Therefore, we shall abandon the weighted N-scheme approach and will not discuss it further in the paper. However, the 'weighted' idea will be applied on the LDA. □

Appendix 5: Grid Topology

Isotropic Grid

The isotropic grid is an unstructured-type grid with right triangular elements. In order to control the skewness one could use the ratio of two right angle edges as shown in Fig. 33. The relation between the stretching parameter ($s = \frac{k}{h}$) and the skewness is shown in the next equation, although its derivation is omitted here for brevity. The details can be found in [12].

$$Q = \frac{2}{\pi}\arctan\left(\frac{s}{2}\right) \tag{71}$$

Note that the minimum value for s will be 1. Substituting $s = 1$, the minimum value for the skewness will be $Q \simeq 0.3$ which is for right triangles. In other words, the best condition for isotropic grid would be having skewness of 0.3.

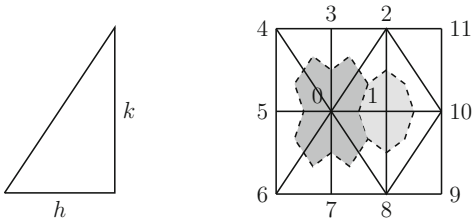

Fig. 33 The isotropic grid element and topology for RD and FV methods (finite volume cells are *shaded*)

The grid skewness will be determined by setting the stretching parameter. In this grid type there are two kinds of points, one with eight neighboring elements and one with four neighbors. Note that, for the finite volume cell vertex the median points of the neighboring cells and midpoints of the edges are used to demonstrate the cell. Thus, the outer of a finite volume cell is depended on the arrangement of the neighboring cells. For the first and second type of isotropic grids, the finite volume cell vertex element is shaded in Fig. 33. It is much easier to handle the isotropic grids in terms of achieving a uniformly skewed grids over the whole computational domain and also when doing the mathematical analyses. As such, the isotropic grids are used for scalar problems where rigorous mathematical analyses would be performed.

Anisotropic Grid

The Delaunay triangulation is used to generate a fully unstructured or anisotropic grid over a cylinder. After generating the grid it would be randomized the in a way that different quality of the grids in terms of skewness could be built. This is where achieving a uniform grid skewness over the complete domain would not be possible but rather the grid skewness would have a range (or distribution). It should be mentioned that each randomization construct a different skewness distribution. Since the elements are not necessarily right triangular elements (unlike isotropic), the skewness ranges from 0 to 1.0.

According to Fig. 34, each point will move in fully randomize direction with a finite maximum distance (R) which avoids grid overlapping.

- The randomization percentage: The maximum distance that a point can move from its original place is R which we can be controlled in terms of percentage defined as $\alpha \times R$. A suitable value for α is chosen to implement grid irregularity. Larger values of α denote a higher percentage grid randomization.
- Randomization number: To build a much more realistic unstructured grid one could perform the whole process (n) times, to build even more randomized grid.

The two options above might be written as (α, n). It should be mentioned that in this study, we are using three different combination of randomization to cover the possibilities in the engineering problems which are $(20\%, 2)$, $(50\%, 5)$ and $(90\%, 9)$. For simplicity, we are

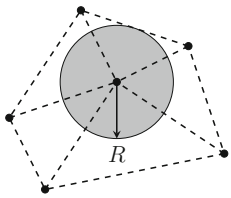

Fig. 34 The randomize grid element area with radius of the minimum distance of the each point from the surrounding edges

calling these three randomization grids as $G1$, $G2$ and $G3$. The anisotropic grids will only be used when solving the system of Euler equations.

Showing Zero Weight for One Characteristic Projection

Lemma 7.2 *At least one of the ratios in* Eq. 27 *for a specific edge number e is zero but the summation is always one.*

Proof The minimum value of $\vec{N}_i \cdot \vec{N}_p$ could be found by $p = i, j, k$. Consider $p = i$ then,

$$\frac{A_i}{A^\tau} = \frac{1}{3} - \frac{\vec{N}_i \cdot \vec{N}_i}{3\left(\vec{N}_i \cdot \vec{N}_i\right)} = 0 \tag{72}$$

If $p = j$, then,

$$\frac{A_j}{A^\tau} = \frac{1}{3} - \frac{\vec{N}_i \cdot \vec{N}_j}{3\left(\vec{N}_i \cdot \vec{N}_j\right)} = 0 \tag{73}$$

And, if $p = k$, then,

$$\frac{A_k}{A^\tau} = \frac{1}{3} - \frac{\vec{N}_i \cdot \vec{N}_k}{3\left(\vec{N}_i \cdot \vec{N}_k\right)} = 0 \tag{74}$$

Moreover, it is obvious that,

$$\sum_p \frac{A_p}{A^\tau} = \frac{A_i}{A^\tau} + \frac{A_j}{A^\tau} + \frac{A_k}{A^\tau} = 1, \quad p = i, j, k. \tag{75}$$

□

References

1. Hall, M.: Cell vertex multigrid schemes for the solution of the euler equations. Numer. Fluids Fluid Dyn. **II**, 303–365 (1886)
2. Morton, K., Crumpton, P., Mackenzie, J.: Cell vertex methods for inviscid and viscous flows. J. Comput. Fluids **22**(2,3), 91–102 (1993)
3. Morton, K., Rudgyard, M.A., Shaw, G.J.: Upwind iteration methods for the cell vertex scheme in one-dimension. J. Comput. Phys. **114**(2), 209–226 (1994)
4. Roe, P. L.: Fluctuations and signals, a framework for numerical evolution problems. Numer. Methods Fluid Dyn. **11**, 219–257 (1982)
5. Abgrall, R.: An extension of roe's upwind scheme to algebraic equilibrium real gas models. Comput. Fluids **19**(2), 171–182 (1991)
6. Abgrall, R.: Toward the ultimate conservative scheme: following the quest. J. Comp. Phys. **167**(2), 277–315 (2001)
7. Abgrall, R.: Residual distribution schemes: current status and future trends. Comput. Fluids **35**(7), 641–669 (2006)
8. Abgrall, R., Trefilík, J.: An example of high order residual distribution scheme using non-lagrange elements. J. Sci. Comput. **45**(1–3), 3–25 (2010)
9. Deconinck, H., Struijs, R., Bourgois, G., Roe, P.L.: Compact advection schemes on unstructured grids. In: Computational Fluid Dynamics, VKI LS 1993-04 (1993)
10. Mesaros, L.M.: Fluctuation Splitting Schemes for the Euler Equations on Unstructured Grid, Ph.D. thesis, University of Michigan (1995)
11. Nishikawa, H.: Robust and accurate viscous discretization via upwind scheme I: basic principle. Comput. Fluids **49**(1), 62–86 (2011)

12. Chizari, H., Ismail, F.: Accuracy variations in residual distribution and finite volume methods on triangular grids. Bull. Malays. Math. Sci. Soc. **22**, 1–34 (2015)
13. Guzik, S., Groth, C.: Comparison of solution accuracy of multidimensional residual distribution and godunov-type finite-volume methods. Int. J. Comp. Fluid Dyn. **22**, 61–83 (2008)
14. De Santis, D.: High-order linear and non-linear residual distribution schemes for turbulent compressible flows. Comput. Methods Appl. Mech. Eng. **285**, 1–31 (2015)
15. Koloszar, L., Villedieu, N., Quintino, T., Rambaud, P., Deconinck, H., Anthoine, J.: Residual distribution method for aeroacoustics. AIAA J. **49**(5), 1021–1037 (2011)
16. Mazaheri, A., Nishikawa, H.: Improved second-order hyperbolic residual-distribution scheme and its extension to third-order on arbitrary triangular grids. J. Comp. Phys. **300**(1), 455–491 (2015)
17. van der Weide, E.: Compressible flow simulation on unstructured grids using multidimensional upwind schemes, Ph.D. thesis, Delft University of Technology (1998)
18. Zienkiewicz, O.C., Taylor, R.L. Zhu, J.: The finite element method: its basis and fundamentals, 6th edn. Elsevier (2005)
19. Deconinck, H., Sermeus, K., Abgrall, R.: Status of multidimensional upwind residual distribution schemes and applications in aeronautics. Fluids 2000 Conference and Exhibit, Denver
20. Abgrall, R., Mezine, M.: Residual distribution scheme for steady problems. In 33rd Computational Fluid Dynamics Course VKI Lecture Series 2003–20005 (Von Karman Institute for Fluid Dynamics)
21. Dobes, J., Deconinck, H.: Second order blended multidimensional upwind residual distribution scheme for steady and unsteady computations. J. Comput. Appl. Math. **215**(2), 378–389 (2008)
22. Abgrall, R.: A review of residual distribution schemes for hyperbolic and parabolic problems: the July 2010 state of the art. Commun. Comp. Phys. **11**(4), 1043–1080 (2012)
23. Masatsuka, K.: I do like CFD, book, Vol. 1 (2009)
24. Blazek, J.: Computational fluid dynamics: principles and applications (2001)
25. Roe, P.L.: Approximate Riemann solvers, parameter and difference schemes. J. Comput. Phys. **43**, 357–372 (1981)